

# Minimum-Time Trajectory Optimization of Low-Thrust Earth-Orbit Transfers with Eclipsing

Kathryn F. Graham\*  
Anil V. Rao†

*University of Florida  
Gainesville, FL 32611-6250*

## Abstract

The problem of determining high-accuracy minimum-time Earth-orbit transfers using low-thrust propulsion with eclipsing is considered. The orbit transfer problem is posed as a multiple-phase optimal control problem where the spacecraft can thrust only during phases where it has line of sight to the sun. Event constraints, based on the geometry of a penumbra shadow region, are enforced between the phases and determine the amount of time spent in an eclipse. An initial guess generation method is developed that constructs a useful guess by solving a series of single-phase optimal control problems and analyzing the resulting trajectory to approximate where the spacecraft enters and exits the Earth's shadow. The single-phase and multiple-phase optimal control problems are solved using an *hp* adaptive Legendre-Gauss-Radau orthogonal collocation method. To demonstrate the effectiveness of the approach developed in this research, optimal transfer trajectories are computed for two Earth-orbit transfers found in the literature. In addition to the two comparison cases studied, a separate Earth-orbit transfer is examined, and solutions are presented for four different departure dates.

## Nomenclature

$a$	=	Semi-major Axis, m
$e$	=	Eccentricity
$f$	=	Second Modified Equinoctial Element
$g$	=	Third Modified Equinoctial Element
$g_e$	=	Sea Level Acceleration Due to Earth Gravity, m/s <sup>2</sup>
$h$	=	Second Modified Equinoctial Element
$i$	=	Inclination, deg or rad
$(\mathbf{i}_r, \mathbf{i}_\theta, \mathbf{i}_h)$	=	Rotating Radial Coordinate System
$J_2$	=	Second Zonal Harmonic
$J_3$	=	Third Zonal Harmonic
$J_4$	=	Fourth Zonal Harmonic
$k$	=	Fifth Modified Equinoctial Element
$L$	=	Sixth Modified Equinoctial Element (True Longitude), rad or deg
$m$	=	Mass, kg
$n$	=	Mean Motion

---

\*Ph.D. Candidate, Department of Mechanical and Aerospace Engineering. E-mail: kschuber@ufl.edu.

†Associate Professor, Department of Mechanical and Aerospace Engineering. E-mail: anilvr Rao@ufl.edu. Associate Fellow, AIAA. Corresponding Author.

It is noted that a highly preliminary version of this research was presented as Paper AAS 14-438 at the 2015 AAS/AIAA Space Flight Mechanics Meeting held in Williamsburg, Virginia, 11 - 15 January 2015.

$P$	=	Input Power, kW
$P_k$	=	Legendre Polynomial of Degree $k$
$p$	=	First Modified Equinoctial Element (Semi-Parameter), m
$R_e$	=	Radius of the Earth, m
$R_s$	=	Radius of the Sun, m
$T$	=	Thrust, N
$t$	=	Time, s or d
$\mathbf{u}$	=	Control Direction
$u_r$	=	Radial Component of Control
$u_\theta$	=	Tangential Component of Control
$u_h$	=	Normal Component of Control
$\Delta$	=	Spacecraft Specific Force, $\text{m}\cdot\text{s}^{-2}$
$\eta$	=	Thruster Efficiency, %
$\mu_e$	=	Earth Gravitational Parameter, $\text{m}^3\cdot\text{s}^{-2}$
$\mu_s$	=	Sun Gravitational Parameter, $\text{m}^3\cdot\text{s}^{-2}$
$\nu$	=	True Anomaly, deg or rad
$\Omega$	=	Longitude of Ascending Node, deg or rad
$\omega$	=	Argument of Periapsis, deg or rad

## 1 Introduction

The use of low-thrust propulsion has been studied extensively for orbital rendezvous, orbit maintenance, orbit transfer, and interplanetary space mission applications. While the efficiency of low-thrust propulsion is highly appealing for a variety of applications, the corresponding problem is computationally challenging to solve. For instance, when using low-thrust propulsion to perform Earth-orbit transfers, the high specific impulse combined with a small specific force leads to very long transfer times. In addition, the trajectory design problem is especially complicated if the initial and terminal orbits are widely spaced because a large number of orbital revolutions are necessary to complete the transfer. Furthermore, if the low-thrust propulsion system is powered by solar panels, thrust is not available when the spacecraft passes through the Earth's shadow and therefore the trajectory design problem must be segmented into a number of phases. The result is a multiple-phase optimal control problem that is very challenging to solve.

Low-thrust trajectory optimization of Earth-orbit transfers has been studied over the past several decades. Ref. [1] employs optimal control theory to solve minimum-time, circle-to-circle, constant thrust orbit raising to generate simple graphical and analytical tools to relate vehicle design parameters to orbit design parameters. In other literature, a variety of approximation methods have been developed to overcome the computational challenges associated with the large number of orbital revolutions typical of a low-thrust orbital transfer. One of the most common approximation techniques is orbital averaging where simple approximations are derived to express incremental changes in the orbital elements over each orbital revolution. Using orbital averaging, Ref. [2] considered the problem of minimum-fuel power-limited transfers between coplanar elliptic orbits. More recently, in Ref. [3] an orbital averaging approach was developed in conjunc-

tion with hybrid control formulations to solve low-Earth orbit (LEO) to geostationary orbit (GEO) and geostationary transfer orbit (GTO) to GEO transfers. Next, Ref. [4] solved a 100-revolution LEO to GEO coplanar transfer using direct collocation paired with a Runge-Kutta parallel-shooting scheme, while Ref. [5] combined a single shooting method with a homotopic approach to solve a minimum-fuel transfer from a low, elliptic, and inclined orbit to GEO. In order to increase accuracy over orbital averaging techniques, Ref. [6] utilized sequential quadratic programming (SQP) to solve a minimum-fuel, low-thrust, near-polar Earth-orbit transfer with over 578 revolutions. In Ref. [7] an anti-aliasing method utilizing direction collocation was developed to obtain solutions to simple low-thrust trajectory optimization problems. Finally, Ref. [8] addressed minimum-time transfers using direct collocation for a range of initial thrust accelerations and constant specific impulse values.

While many authors have proposed techniques for solving low-thrust trajectory optimization problems, only a few have addressed the problem assuming a solar powered propulsion system. Using solar electric propulsion leads to a fundamentally different and more complex optimal control problem than the well-studied continuous thrust case because Earth-shadow regions must be included in the physical model. References [9, 10, 11] determined Earth-shadow entry and exit points by finding the intersection between the osculating elliptical orbit and a cylindrical shadow model [12]. Using control parameterization and orbital averaging coupled with a direct optimization technique, Refs. [9, 10, 11] solved several Earth-orbit transfers. Cylindrical shadow models and orbital averaging techniques are also used in Refs. [13] and [14], where in Ref. [14] a shooting algorithm is employed to solve neighboring problems developed to avoid the discontinuous behavior associated with the spacecraft entering and exiting a shadow region. Furthermore, Ref. [15] addressed low-thrust zero-eccentricity-constrained orbit raising in a circular orbit, Ref. [16] analyzed low-thrust tangential thrusting along small-to-moderate eccentricity orbits, and Ref. [17] examined low-thrust inclination changes in a near-circular orbit using a cylindrical Earth-shadow model. More recently, Ref. [18] formulated a direct optimization approach that solves a series of large-scale multiple-phase optimal control problems and uses penumbra geometry to determine the shadow entrance and exit locations.

The goal of this research is to develop an approach for computing high-accuracy solutions to low-thrust orbit transfers using solar electric propulsion. The problem is formulated as a multiple-phase optimal control problem that consists of only burn phases. An intelligent initial guess is constructed by solving a series of single-phase optimal control problems and analyzing the solutions to determine approximate shadow entrance and exit locations. The corresponding multiple-phase optimal control problem is then solved using an *hp* adaptive Gaussian quadrature orthogonal collocation method [19, 20, 21, 22, 23, 24, 25, 26] with the software `GPOPS – III` as described in Ref. [26]. Using the approach of this paper, solutions to the multiple-phase optimal control problem are obtained without replacing the equations of motion with

averaged approximations over each orbital revolution (such as when orbital averaging is employed). The multiple-phase optimal control problem consists of thrust phases and event constraints that account for changes in the orbit from the entrance to the exit of each shadow region, where the shadow regions are determined from the geometry of the problem. By employing event constraints in this manner, the change in the orbit during a non-thrusting shadow segment can be determined without having to model the shadow segment as its own phase, thus eliminating shadow phases from the optimal control problem. The approach developed in this paper is applied to two Earth-orbit transfers found in the literature as well as an Earth-orbit transfer that has not previously been studied in detail.

This paper is organized as follows. In Section 2 the problem formulation is provided. In particular, Section 2 provides the differential equations that describe the motion of the spacecraft, the boundary conditions, the path constraints, the definition of a shadow region, and a description of the resulting multiple-phase low-thrust orbit transfer optimal control problem. In Section 3 the key results are provided along with a discussion of the results. Finally, in Section 4 conclusions on this research are provided.

## 2 Problem Description

Consider the problem of transferring a spacecraft from an initial Earth-orbit to a final Earth-orbit using solar electric propulsion. The objective is to determine the minimum-time trajectory and control inputs that transfer the spacecraft from the specified initial orbit to the specified terminal orbit. In the remainder of this section the details of the low-thrust orbit transfer optimal control problem that employs a model for solar electric propulsion is described.

### 2.1 Equations of Motion

The dynamics of the spacecraft, modeled as a point mass, are described using modified equinoctial elements  $(p, f, g, h, k, L)$  (see Ref. [27]) where  $p$  is the semi-parameter,  $f$  and  $g$  are elements that describe the eccentricity,  $h$  and  $k$  are elements that describe the inclination, and  $L$  is the true longitude. The state of the spacecraft is then given as  $(p, f, g, h, k, L, m)$ , where  $m$  is the vehicle mass. The control is the thrust direction,  $\mathbf{u}$ , where  $\mathbf{u}$  is expressed in rotating radial coordinates as  $\mathbf{u} = (u_r, u_\theta, u_h)$ . A fourth-order oblate gravity model is used and the thrust magnitude is assumed constant when the spacecraft is not in an eclipse.

The differential equations of motion of the spacecraft are then given as

$$\begin{aligned}
\frac{dp}{dt} &= \sqrt{\frac{p}{\mu_e}} \frac{2p}{q} \Delta_\theta \equiv F_p, \\
\frac{df}{dt} &= \sqrt{\frac{p}{\mu_e}} \left( \sin L \Delta_r + \frac{1}{q} \left( (q+1) \cos L + f \right) \Delta_\theta - \frac{g}{q} \left( h \sin L - k \cos L \right) \Delta_h \right) \equiv F_f, \\
\frac{dg}{dt} &= \sqrt{\frac{p}{\mu_e}} \left( -\cos L \Delta_r + \frac{1}{q} \left( (q+1) \sin L + g \right) \Delta_\theta + \frac{f}{q} \left( h \sin L - k \cos L \right) \Delta_h \right) \equiv F_g, \\
\frac{dh}{dt} &= \sqrt{\frac{p}{\mu_e}} \frac{s^2 \cos L}{2q} \Delta_h \equiv F_h, \\
\frac{dk}{dt} &= \sqrt{\frac{p}{\mu_e}} \frac{s^2 \sin L}{2q} \Delta_h \equiv F_k, \\
\frac{dL}{dt} &= \sqrt{\frac{p}{\mu_e}} \left( h \sin L - k \cos L \right) \Delta_h + \sqrt{\mu_e p} \left( \frac{q}{p} \right)^2 \equiv F_L, \\
\frac{dm}{dt} &= -\frac{T}{g_e I_{sp}} \equiv F_m,
\end{aligned} \tag{1}$$

where

$$\begin{aligned}
q &= 1 + f \cos L + g \sin L, & r &= p/q, \\
\alpha^2 &= h^2 - k^2, & s^2 &= 1 + \sqrt{h^2 + k^2}.
\end{aligned} \tag{2}$$

In this research, the true longitude is used as the independent variable instead of time. Denoting differentiation with respect to true longitude by  $(\cdot)'$ , the differential equation for  $t$  is given as

$$t' = \frac{dt}{dL} = \frac{1}{F_L} = F_L^{-1} \equiv G_t, \tag{3}$$

while the remaining six differential equations for  $(p, f, g, h, k, m)$  that describe the dynamics of the spacecraft are given as

$$(p, f, g, h, k, m)' = F_L^{-1} (F_p, F_f, F_g, F_h, F_k, F_m) \equiv (G_p, G_f, G_g, G_h, G_k, G_m). \tag{4}$$

Next, the spacecraft acceleration,  $\Delta = (\Delta_r, \Delta_\theta, \Delta_h)$ , is modeled as

$$\Delta = \Delta_g + \Delta_T, \tag{5}$$

where  $\Delta_g$  is the gravitational acceleration due to the oblateness of the Earth and  $\Delta_T$  is the thrust specific force. The acceleration due to Earth oblateness is expressed in rotating radial coordinates as

$$\Delta_g = \mathbf{Q}_r^T \delta \mathbf{g}, \tag{6}$$

where  $\mathbf{Q}_r = [\mathbf{i}_r \quad \mathbf{i}_\theta \quad \mathbf{i}_h]$  is the transformation from rotating radial coordinates to Earth-centered inertial coordinates and whose columns are defined as

$$\mathbf{i}_r = \frac{\mathbf{r}}{\|\mathbf{r}\|}, \quad \mathbf{i}_h = \frac{\mathbf{r} \times \mathbf{v}}{\|\mathbf{r} \times \mathbf{v}\|}, \quad \mathbf{i}_\theta = \mathbf{i}_h \times \mathbf{i}_r. \tag{7}$$

Furthermore, the vector  $\delta \mathbf{g}$  is defined as

$$\delta \mathbf{g} = \delta g_n \mathbf{i}_n - \delta g_r \mathbf{i}_r \quad (8)$$

where  $\mathbf{i}_n$  is the local North direction and is defined as

$$\mathbf{i}_n = \frac{\mathbf{e}_n - (\mathbf{e}_n^T \mathbf{i}_r) \mathbf{i}_r}{\|\mathbf{e}_n - (\mathbf{e}_n^T \mathbf{i}_r) \mathbf{i}_r\|} \quad (9)$$

and  $\mathbf{e}_n = (0, 0, 1)$ . The oblate earth perturbations are then expressed as

$$\delta g_r = -\frac{\mu_e}{r^2} \sum_{k=2}^4 (k+1) \left( \frac{R_e}{r} \right)^k P_k(\sin \phi) J_k, \quad (10)$$

$$\delta g_n = -\frac{\mu_e \cos \phi}{r^2} \sum_{k=2}^4 \left( \frac{R_e}{r} \right)^k P'_k(\sin \phi) J_k, \quad (11)$$

where  $R_e$  is the equatorial radius of the earth,  $P_k$  is the  $k^{th}$ -degree Legendre polynomial,  $P'_k$  is the derivative of  $P_k$  with respect to  $\sin \phi$ , and  $J_k$  represents the zonal harmonic coefficients for  $k = (2, 3, 4)$ . Next, the thrust specific force is given as

$$\Delta_T = \frac{T}{m} \mathbf{u} \quad (12)$$

where  $T$  is defined as

$$T = \frac{2\eta P}{g_e I_{sp}}. \quad (13)$$

(To further improve the accuracy of the solutions obtained in this study, the spacecraft acceleration model should also include the effects of solar gravitational perturbations, lunar gravitational perturbations, and solar radiation pressure. These additional perturbations, however, were outside the scope of this research.)

Finally, the physical constants used in this study are given in Table 2.

Table 2: Physical Properties.

Constant	Value
$g_e$	9.80665 m · s <sup>-2</sup>
$R_e$	6378140 m
$\mu_e$	$3.9860047 \times 10^{14}$ m <sup>3</sup> · s <sup>-2</sup>
$R_s$	695500000 m
$\mu_s$	$1.32712440018 \times 10^{20}$ m <sup>3</sup> · s <sup>-2</sup>
$J_2$	$1082.639 \times 10^{-6}$
$J_3$	$-2.565 \times 10^{-6}$
$J_4$	$-1.608 \times 10^{-6}$

## 2.2 Boundary Conditions and Path Constraints

The boundary conditions for the orbit transfer are described in terms of both classical orbital elements and modified equinoctial elements. The initial orbit is specified in terms of classical orbital elements [28] as

$$\begin{aligned} a(L_0) &= a_0, & \Omega(L_0) &= \Omega_0, \\ e(L_0) &= e_0, & \omega(L_0) &= \omega_0, \\ i(L_0) &= i_0, & \nu(L_0) &= \nu_0, \end{aligned} \tag{14}$$

where  $a$  is the semi-major axis,  $e$  is the eccentricity,  $i$  is the inclination,  $\Omega$  is the longitude of the ascending node,  $\omega$  is the argument of periapsis, and  $\nu$  is the true anomaly. Equation (14) can be expressed equivalently in terms of the modified equinoctial elements as

$$\begin{aligned} p(L_0) &= a_0(1 - e_0^2), & h(L_0) &= \tan(i_0/2) \sin \Omega_0, \\ f(L_0) &= e_0 \cos(\omega_0 + \Omega_0), & k(L_0) &= \tan(i_0/2) \cos \Omega_0, \\ g(L_0) &= e_0 \sin(\omega_0 + \Omega_0), & L_0 &= \Omega_0 + \omega_0 + \nu_0. \end{aligned} \tag{15}$$

The terminal orbit used in this research is specified in classical orbital elements as

$$\begin{aligned} a(L_f) &= a_f, & \Omega(L_f) &= \text{Free}, \\ e(L_f) &= e_f, & \omega(L_f) &= \text{Free}, \\ i(L_f) &= i_f, & \nu(L_f) &= \text{Free}. \end{aligned} \tag{16}$$

Equation (16) can be expressed equivalently in terms of the modified equinoctial elements as

$$\begin{aligned} p(L_f) &= a_f(1 - e_f^2), \\ \left( f^2(L_f) + g^2(L_f) \right)^{1/2} &= e_f, \\ \left( h^2(L_f) + k^2(L_f) \right)^{1/2} &= \tan(i_f/2). \end{aligned} \tag{17}$$

Finally, during the transfer the thrust direction must be a vector of unit length. Thus, the equality path constraint

$$\|\mathbf{u}\|_2 = u_r^2 + u_\theta^2 + u_h^2 = 1 \tag{18}$$

is enforced throughout all phases of the transfer where the spacecraft is allowed to thrust.

## 2.3 Model for Solar Electric Propulsion

In this section a model is described for a spacecraft that uses solar electric propulsion. In this model it is assumed that the spacecraft applies maximum thrust when it has line of sight to the Sun and applies zero thrust when line of sight to the Sun is lost. The model consists of two parts. In the first part of the model

a shadow region (an eclipse), that is, a segment of the solution where line of sight to the Sun is lost, is described. In the second part of the model the conditions that define a start and a terminus of a shadow region are described along with the conditions that define the change in the location of the spacecraft as it moves from an entrance to an exit of a shadow region.

### 2.3.1 Definition of a Shadow Region

By calculating the position of the Sun,  $\mathbf{s}$ , throughout the transfer, the penumbra and umbra shadow regions can be defined. Low precision formulas were employed to efficiently determine the coordinates of the Sun in equatorial rectangular coordinates [29]. (The low precision formulas give the coordinates of the Sun to a precision of 1/100 deg and the equation of time to a precision of 3.5 s between 1950 and 2050.) If a solar powered spacecraft travels through a penumbra region, the propulsion system will receive limited solar energy, while passage through an umbra region will result in a complete loss of solar energy.

In a manner similar to Ref. [30], the celestial bodies are assumed to be spherical which generates shadow regions that are conical projections. In this approach, only a penumbra shadow region is considered and the thrust of the spacecraft is assumed to be zero when traveling through the shadow region. The penumbra cone geometry is shown in Fig. 1, where the distance between point  $P$  and the center of the earth is defined as

$$\chi_p = \frac{R_e d_p}{R_e + R_s} \quad (19)$$

and the angle  $\alpha_p$  is defined as

$$\alpha_p = \sin^{-1} \left( \frac{R_e}{\chi_p} \right). \quad (20)$$

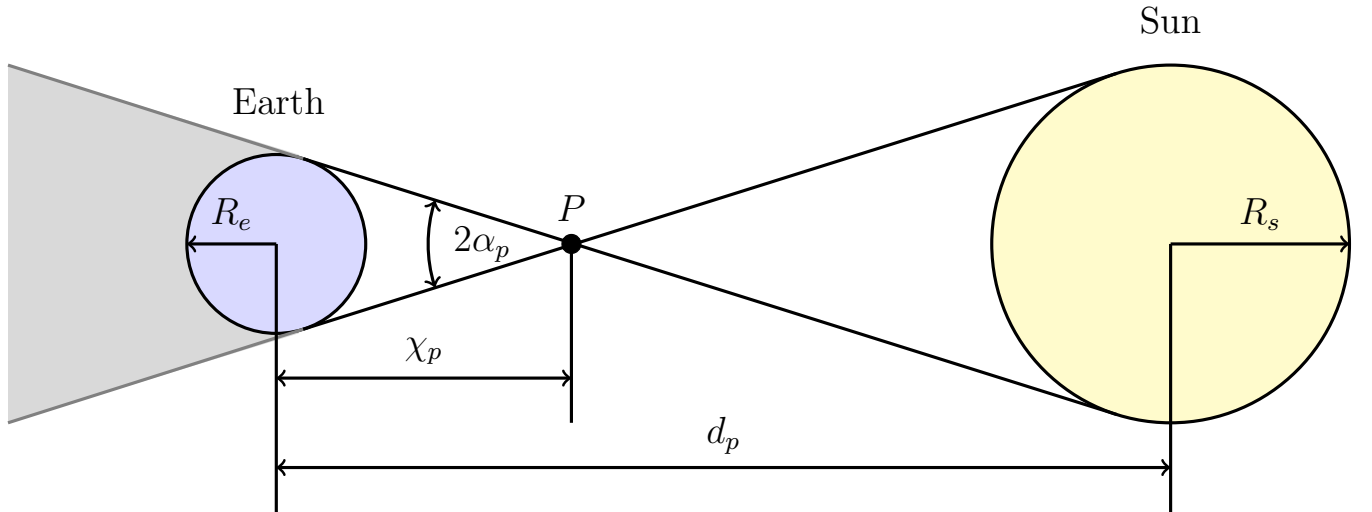


Figure 1: Penumbra cone geometry.

The projected spacecraft location is then utilized to locate the penumbra cone terminators. Figure 2



shows the projected spacecraft location geometry, where the location of the spacecraft,  $\mathbf{r}$ , is defined as

$$\mathbf{r} = \begin{bmatrix} \frac{r}{s^2}(\cos L + \alpha^2 \cos L + 2hk \sin L) \\ \frac{r}{s^2}(\sin L - \alpha^2 \sin L + 2hk \cos L) \\ \frac{2r}{s^2}(h \sin L - k \cos L) \end{bmatrix}. \quad (21)$$

The solar unit vector

$$\hat{\mathbf{s}} = \frac{\mathbf{s}}{\|\mathbf{s}\|} \quad (22)$$

is utilized to determine the projection of the spacecraft along  $\hat{\mathbf{s}}$  which is defined as

$$\mathbf{r}_p = (\mathbf{r} \cdot \hat{\mathbf{s}})\hat{\mathbf{s}}. \quad (23)$$

The distance between the center of the penumbra cone and the spacecraft at the projection point is defined as

$$\boldsymbol{\delta} = \mathbf{r} - \mathbf{r}_p, \quad (24)$$

and the distance between the center of the penumbra cone and the penumbra terminator point at the projected spacecraft location is defined as

$$\kappa = (\chi_p + \|\mathbf{r}_p\|) \tan \alpha_p. \quad (25)$$

A comparison of the distance  $\kappa$  with the magnitude of the vector  $\boldsymbol{\delta}$  determines the shadow terminator points as described below:

1. Shadow terminator points are only feasible if  $\mathbf{r} \cdot \hat{\mathbf{s}} < 0$ . However, if  $\|\boldsymbol{\delta}\| > \kappa$ , the spacecraft is still in Sunlight.
2. Penumbra terminator points occur when  $\|\boldsymbol{\delta}\| = \kappa$  and the spacecraft is in the penumbra cone if  $\|\boldsymbol{\delta}\| < \kappa$ .

### 2.3.2 Event Constraints Defining Entrance and Exit of a Shadow Region

The following event constraints define the entrance and exit of a shadow region. First, because the duration of coasting flight during an eclipse is less than one third of an orbital period, it is assumed during an eclipse that the spacecraft is under the influence of central body gravity (that is, Keplerian motion). As a result, the first five modified equinoctial elements  $(p, f, g, h, k)$  are constant during an eclipse and the only modified equinoctial element that changes is the true longitude,  $L$ . Next, let  $\Delta L^{(r)}$  be optimization parameters that define the change in true longitude during the  $r^{th}$  eclipse (where  $r = 1, \dots, R - 1$  and  $R$  is the number

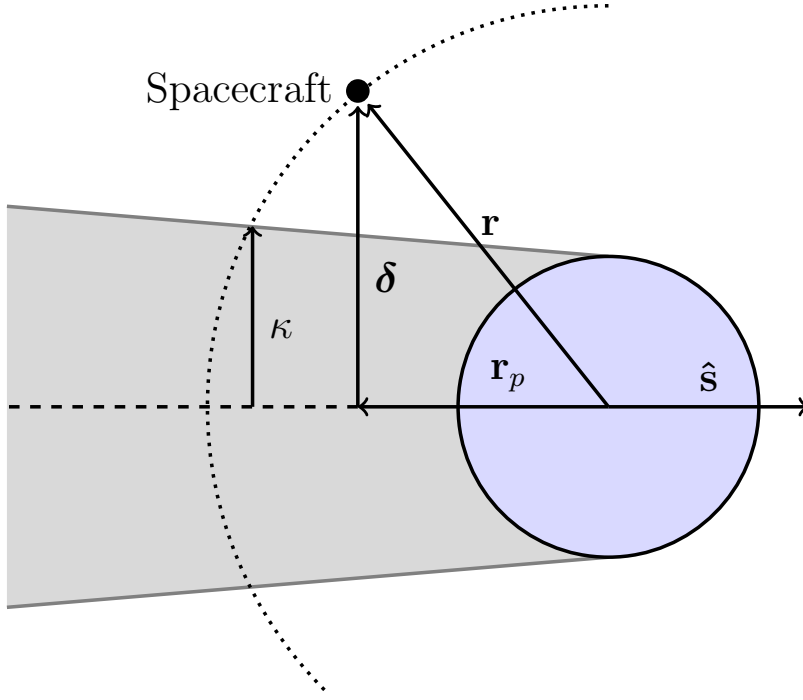


Figure 2: Projected spacecraft location geometry.

of phases). Because the duration of the eclipse is less than one third of an orbital period, the following constraint is placed on  $\Delta L^{(r)}$ :

$$0 < \Delta L^{(r)} \leq \pi. \quad (26)$$

The relationship between the longitude at the start and terminus of the  $r^{th}$  eclipse is then given as

$$L_0^{(r+1)} - L_f^{(r)} + \Delta L^{(r)} = 0, \quad (r = 1, \dots, R-1). \quad (27)$$

The duration of the  $r^{th}$  eclipse,  $dt^{(r)}$ , is then obtained by integrating Eq. (3) as

$$t^{(r+1)}(L_0^{(r+1)}) - t^{(r)}(L_f^{(r)}) + \int_{L_f^{(r)}}^{L_0^{(r+1)}} G_t dL = 0, \quad (28)$$

where  $G_t$  is defined in Eq. (3). Recalling that an eclipse occurs only when  $\mathbf{r} \cdot \hat{\mathbf{s}} < 0$ , the endpoints of the initial and all intermediate phases must satisfy

$$\mathbf{r}(L_f^{(r)}) \cdot \hat{\mathbf{s}} < 0, \quad (r = 1, \dots, R-1). \quad (29)$$

Furthermore, an eclipse terminator point can only occur when  $\|\delta\| = \kappa$  as dictated by the geometry of the penumbra cone. Therefore, the endpoints of the initial phase and all intermediate phases must satisfy

$$\|\delta(L_f^{(r)})\| - \kappa = 0, \quad (r = 1, \dots, R-1), \quad (30)$$

while the initial points of all the intermediate phases and terminal phase must satisfy

$$\|\delta(L_0^{(r+1)})\| - \kappa = 0, \quad (r = 1, \dots, R-1). \quad (31)$$

Finally, because the spacecraft is assumed to be under the influence of central body gravitation during an eclipse, the following constraints are imposed on the state components  $(p, f, g, h, k, m)$  at the start and terminus of an eclipse:

$$\begin{aligned}
p^{(r+1)}(L_0^{(r+1)}) - p^{(r)}(L_f^{(r)}) &= 0, \\
f^{(r+1)}(L_0^{(r+1)}) - f^{(r)}(L_f^{(r)}) &= 0, \\
g^{(r+1)}(L_0^{(r+1)}) - g^{(r)}(L_f^{(r)}) &= 0, \\
h^{(r+1)}(L_0^{(r+1)}) - h^{(r)}(L_f^{(r)}) &= 0, \\
k^{(r+1)}(L_0^{(r+1)}) - k^{(r)}(L_f^{(r)}) &= 0, \\
m^{(r+1)}(L_0^{(r+1)}) - m^{(r)}(L_f^{(r)}) &= 0.
\end{aligned} \tag{32}$$

It is emphasized again that Keplerian motion during an eclipse is assumed because the duration of an eclipse is only a small fraction of an orbital period.

## 2.4 Multiple-Phase Optimal Control Problem

The aforementioned Earth-shadow model leads naturally to decomposing the spacecraft motion into phases. Using this aforementioned approach, the structure of the multiple-phase optimal control problem is as follows. The first phase starts with the spacecraft in its initial orbit and terminates when the spacecraft reaches the start of the first shadow region. Each intermediate phase of the multiple-phase optimal control problem corresponds to a segment of the trajectory that begins at an exit point of a shadow and ends at the next shadow entry point. The final phase corresponds to the trajectory segment that begins at the last shadow exit point and ends when the desired terminal orbit is obtained. The multiple-phase optimal control problem arising from the aforementioned low-thrust orbital transfer with eclipsing constraints is then given as follows. Determine the trajectory  $(p(L), f(L), g(L), h(L), k(L), m(L), t(L))$ , the control  $(u_r(L), u_\theta(L), u_h(L))$ , and the event constraint parameters  $\Delta L^{(r)}$ ,  $(r = 1, \dots, R - 1)$ , that minimize the cost functional

$$J = \alpha t_f \tag{33}$$

subject to the dynamic constraints of Eqs. (3) and (4), the initial conditions of Eq. (15), the terminal conditions of Eq. (17), the path constraint of Eq. (18), the parameter constraints of Eq. (26), and the event constraints of Eq. (27)-(32). (Note that  $\alpha = 1/86400$  is the conversion factor from units of seconds to units of days.)

## 2.5 Initial Guess Generation

A single-phase optimal control problem without eclipse constraints (continuous thrust) is solved first to generate a nominal trajectory using the approach described in Ref. [8]. The single-phase optimal control

problem is stated as: Determine the trajectory  $(p(L), f(L), g(L), h(L), k(L), m(L), t(L))$  and the control inputs  $(u_r(L), u_\theta(L), u_h(L))$  that minimize the cost functional

$$J = \alpha t_f, \quad (34)$$

subject to the dynamic constraints of Eqs. (3) and (4), the initial conditions of Eq. (15), the terminal conditions of Eq. (17), and the path constraint of Eq. (18). The nominal trajectory is then analyzed to determine the number of times the spacecraft enters the Earth's shadow which will vary depending on the launch date chosen. The trajectory is initially analyzed to locate the first shadow entry point. The equations of motion are then propagated until a shadow exit point is obtained. The remaining trajectory is adjusted and the single-phase optimal control problem is solved again using initial conditions that correspond to the shadow exit point found by propagating the equations of motion. The resulting nominal trajectory is once again analyzed as before until another shadow entry point is obtained or the desired terminal condition is satisfied. For example, consider an orbit transfer where a spacecraft travels through the Earth's shadow only one time. Analysis of the nominal trajectory would lead to a two phase problem. The first phase will solve for the trajectory from the initial condition to the entry point of the shadow region and the second phase will solve for the trajectory from the exit point of the shadow region to the desired terminal condition.

### 3 Results and Discussion

The multiple-phase low-thrust optimal control orbit transfer problem described in Section 2 was solved using the MATLAB optimal control software `GPOPS – III` [26] with the open-source nonlinear programming problem (NLP) solver IPOPT [31]. `GPOPS – III` employs an *hp*-adaptive Legendre-Gauss-Radau collocation method [24, 23, 32, 33] where the optimal control problem is transcribed into a large sparse NLP and the NLP is solved on successive meshes until a desired accuracy is achieved. In this research the *ph* mesh refinement method described in Ref. [25] is employed with a mesh refinement accuracy tolerance of  $10^{-7}$  and the IPOPT NLP solver tolerance was also set to  $10^{-7}$ . All first and second derivatives required by IPOPT were approximated using the sparse finite-difference derivative approximation method described in Refs. [26] and [32].

To demonstrate the approach, the orbit transfers summarized in Table 3 were computed using the mission characteristics shown in Table 4. Cases 1 and 2 were chosen in order to demonstrate the effectiveness of the approach of this paper against results that have already appeared in the open literature. Case 1 is a transfer from geostationary transfer orbit (GTO) to geostationary orbit (GEO) taken from Refs. [9] and [10], while Case 2 is a slightly different GTO to GEO transfer taken from Ref. [34]. Finally, Case 3 is a super-synchronous transfer orbit (SSTO) to GEO transfer, where the SSTO parameters are characteristic

of an orbit insertion via a Falcon 9 launch vehicle. Case 1 has a departure date of January 1, 2000 at 0:00 UT and Case 2 has a departure date of March 22, 2000 at 0:00 UT. In order to be consistent, Cases 1 and 2 were both solved with the  $J_2$  gravity perturbation only, while Case 3 was solved with  $J_2$  through  $J_4$  gravity perturbations. Moreover, the following departure dates were considered for Case 3: Vernal Equinox (March 20 at 3:50 UT), Summer Solstice (June 20 at 21:44 UT), Autumnal Equinox (September 22 at 13:31 UT), and Winter Solstice (December 21 at 10:02 UT) for the year 2020.

Next, for Cases 2 and 3, the behavior of the optimal control will be explained by analyzing the following three differential equations that describe the evolution of the semi-major axis, eccentricity, and inclination [35]:

$$\frac{da}{dt} = \frac{2e \sin \nu}{nx} u_r + \frac{2ax}{nr} u_\theta, \quad (35)$$

$$\frac{de}{dt} = \frac{x \sin \nu}{na} u_r + \frac{x}{na^2 e} \left( \frac{a^2 x^2}{r} - r \right) u_\theta, \quad (36)$$

$$\frac{di}{dt} = \frac{r \cos(\nu + \omega)}{na^2 x} u_h, \quad (37)$$

where  $n$  is the mean motion and  $x = \sqrt{1 - e^2}$ . It is seen from Eq. (35) that the semi-major axis will increase most rapidly when the control points either in the positive  $u_\theta$  direction, radially outward near  $\nu = \pi/2$  (halfway between periapsis and apoapsis), or radially inward near  $\nu = 3\pi/2$  (halfway between apoapsis and periapsis). The cyclic behavior of  $u_r$  as it relates to Eq. (35) increases apoapsis and decreases periapsis when  $\nu \in [0, \pi]$ , and decreases apoapsis and increases periapsis when  $\nu = [\pi, 2\pi]$ . Furthermore, thrusting radially in this manner increases both the semi-major axis and the eccentricity. On the other hand, from Eq. (36) the eccentricity will decrease most rapidly when the control points either in the positive  $u_\theta$  direction, radially inward near  $\nu = \pi/2$ , or radially outward near  $\nu = 3\pi/2$ . The cyclic behavior of  $u_r$  as it relates to Eq. (36) decreases apoapsis and increases periapsis when  $\nu \in [0, \pi]$ , and increases apoapsis and decreases periapsis when  $\nu = [\pi, 2\pi]$ . Thrusting radially in this manner decreases both the semi-major axis and eccentricity. Finally, it is seen from Eq. (37) that  $di/dt$  is most negative when  $\cos(\nu + \omega)u_h$  is most negative. Therefore, when  $\cos(\nu + \omega)u_h$  is negative, the inclination will decrease.

Table 3: Orbit types.

Orbit	$a, R_e$	$e$	$i, \text{deg}$	$\Omega, \text{deg}$	$\omega, \text{deg}$
GTO-I	3.8200	0.7310	27	99	0
GTO-II	3.8200	0.7306	28.5	0	0
SSTO	8.0785	0.8705	22.5	0	0
GEO	6.6107	0	0	Free	Free

Table 4: Mission characteristics.

Case	$m_0$ , kg	$I_{sp}$ , s	$P$ , kW	$\eta$ , %	Transfer
1	450	3300	5	65	GTO-I to GEO
2	1200	1800	5	55	GTO-II to GEO
3	1200	3300	10	65	SSTO to GEO

### 3.1 Case 1: GTO-I to GEO Transfer Results

Figure 3 shows the optimal GTO-I to GEO trajectory in Earth-centered inertial (ECI) Cartesian coordinates  $(x, y, z)$ , where the Earth-shadow regions are indicated by the grey segments. The multiple-phase optimal control problem contains 89 phases. The Earth-shadow regions appear near periapsis and consequently the spacecraft is in the Earth’s shadow at the start of the transfer. Furthermore, the shadow regions are present throughout the entire transfer and shift away from periapsis towards the ascending node. The spacecraft spends a total of approximately two days in the Earth’s shadow. The optimal solution has a transfer time of 65.9 days, a final mass of 415.71 kg, and completes approximately 89 orbital revolutions.

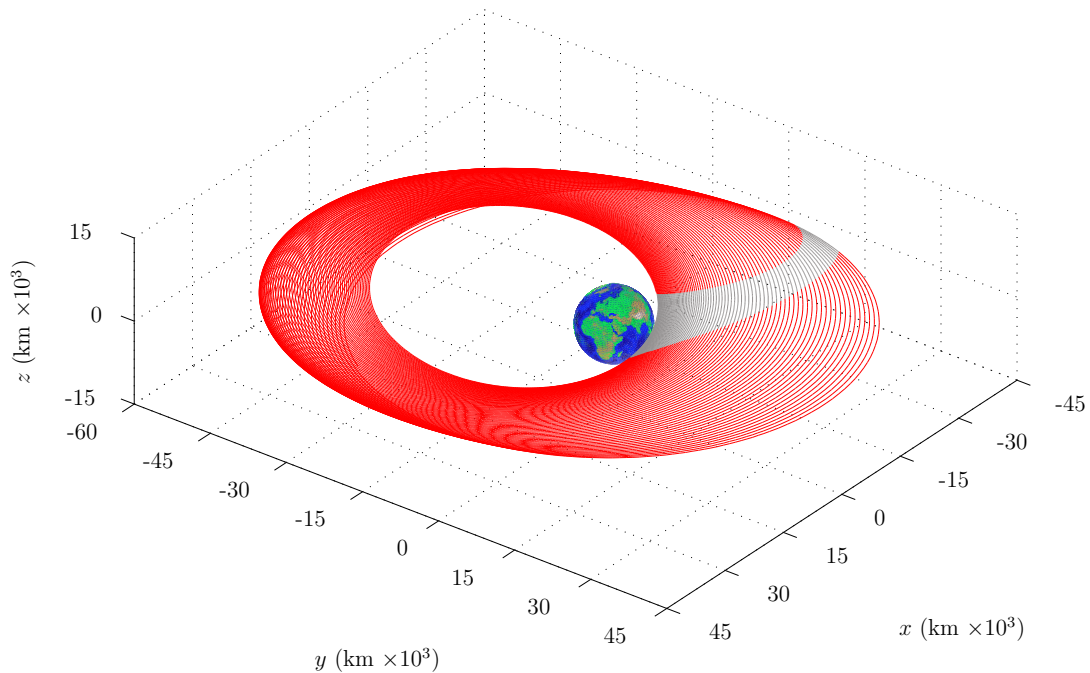


Figure 3: Trajectory for the GTO-I to GEO transfer.

While the optimal transfer time of 65.9 days is similar to the results found in literature, the transfer time obtained in this study is an improvement over previous results. For example, Ref. [9] employs orbital averaging and direct optimization with control parameterization to obtain a transfer time of 67.0 days. Ref. [9] also includes the optimal solution obtained using the software SEPSHOT [36], where SEPSHOT

employs orbital averaging with calculus of variations to obtain an optimal transfer time of 66.6 days. Finally, Ref. [10] employs orbital averaging with parameter optimization to obtain a transfer time of 70.2 days. Thus, the solution obtained in this study has an optimal cost of approximately one day less than the lowest cost obtained in prior research and was obtained using a high accuracy method. While orbital averaging is more computationally efficient when compared to the direct collocation approach of this paper, the errors accumulated by averaging the equations of motion may be large. As a consequence, the spacecraft is unlikely to reach the desired terminal orbit using the control obtained with an orbital averaging approach.

### 3.2 Case 2: GTO-II to GEO Transfer Results

Figure 4 shows the optimal GTO-II to GEO trajectory in ECI Cartesian coordinates  $(x, y, z)$ . The multiple-phase optimal control problem contains 101 phases. The Earth-shadow regions appear near apoapsis at the start of the transfer and slowly shift away from apoapsis towards the descending node. Since the orbital velocity is the smallest near apoapsis, the amount of time spent in the Earth's shadow is quite significant at just over eight days. Moreover, shadow regions do not exist after 59 days. The optimal solution has a final time of 121.22 days, a final mass of 1027.77 kg, and completes approximately 165 orbital revolutions. Next, the time histories of  $a$ ,  $e$ , and  $i$  are shown in Figs. 5a-5c, respectively. It is seen from Fig. 5a that the semi-major axis increases rapidly for the first half of the transfer, then steadily increases to the desired terminal value. Furthermore, it is seen from Fig. 5b that the eccentricity decreases at a slower rate in the first half of the transfer, then rapidly decreases throughout the rest of the transfer. Finally, it is seen from Fig. 5c that the inclination decreases at an approximately linearly rate throughout the transfer.

Next, the optimal transfer time of 121.22 days obtained in this study is in close proximity to the transfer time of 118.36 days obtained in Ref. [34]. Now, while the transfer time obtained in this study is 2.4% larger than the transfer time obtained in Ref. [34], the discrepancy is due to the fact that the approach of this paper differs significantly from the approach used in Ref. [34]. Specifically, the approach of Ref. [34] employs orbital averaging of the equations of motion. Furthermore, Ref. [34] includes only the  $J_2$  gravity perturbation over each orbital revolution and employs a cylindrical Earth-shadow model. Because the equations of motion are replaced by their orbital revolution averages, the solution obtained in Ref. [34] is less accurate than the solution obtained using the direct collocation method of this study. Moreover, averaging the zonal harmonic  $J_2$  has a significant effect on both the longitude of the ascending node and the argument of periapsis, both of which describe the orientation of the orbit and subsequently influence the location in the orbit where an Earth-shadow region appears. Finally, the cylindrical shadow model employed in Ref. [34] will result in smaller shadow regions when compared against the conical projection model employed in this study. Further insight into the structure of the optimal transfer is obtained by examining the optimal control  $\mathbf{u} = (u_r, u_\theta, u_h)$  along different segments of the solution. Figure 6 shows

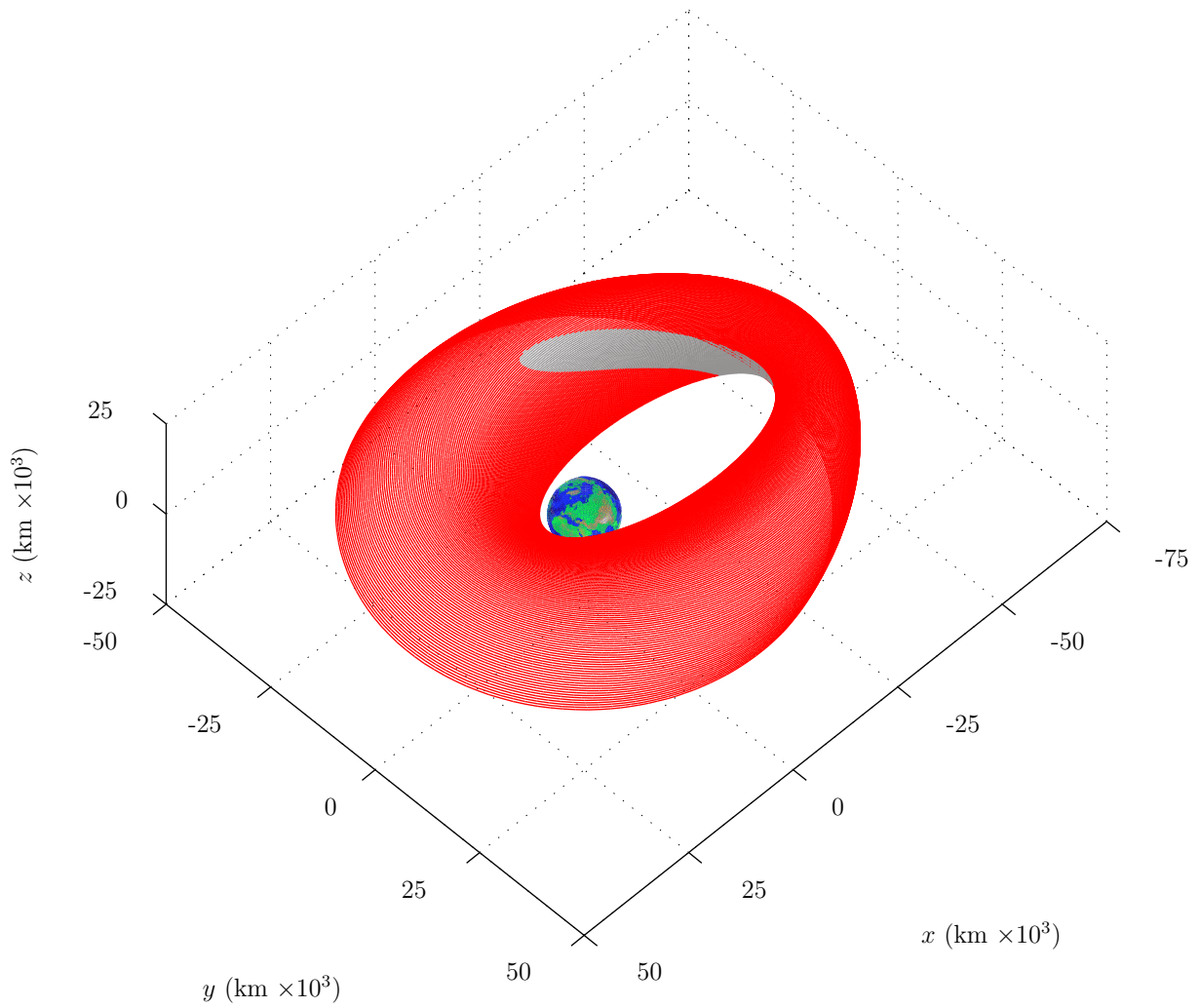
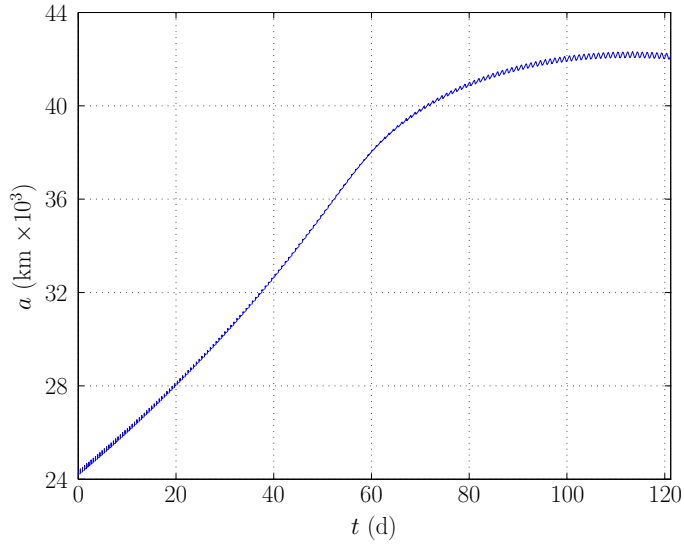
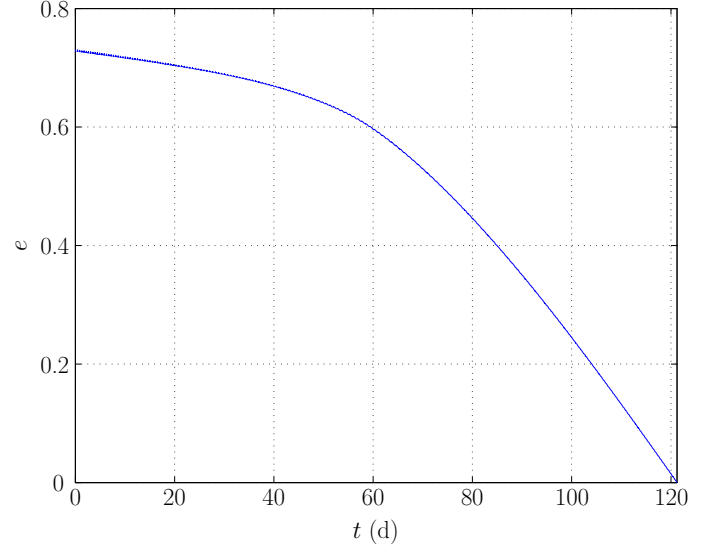


Figure 4: Trajectory for the GTO-II to GEO transfer.

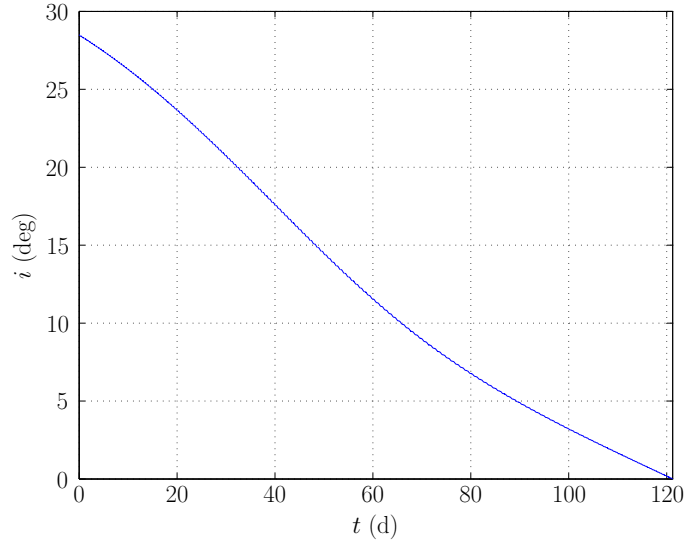




(a)  $a$  vs.  $t$ .



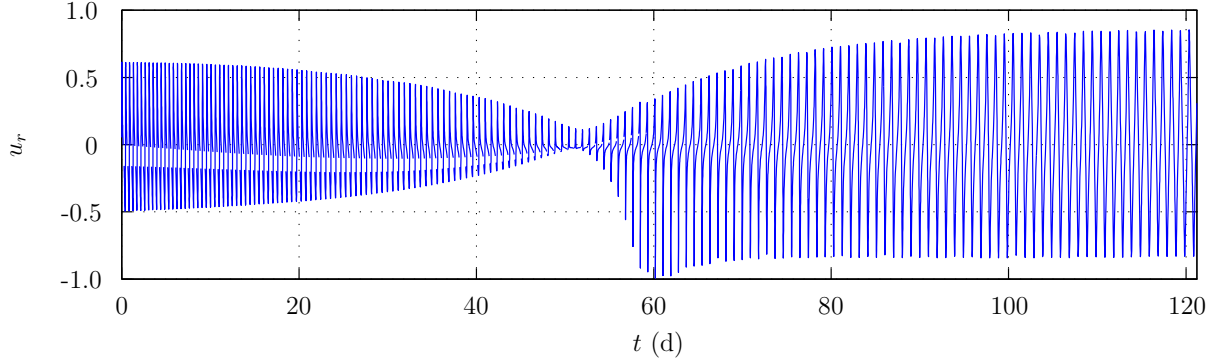
(b)  $e$  vs.  $t$ .



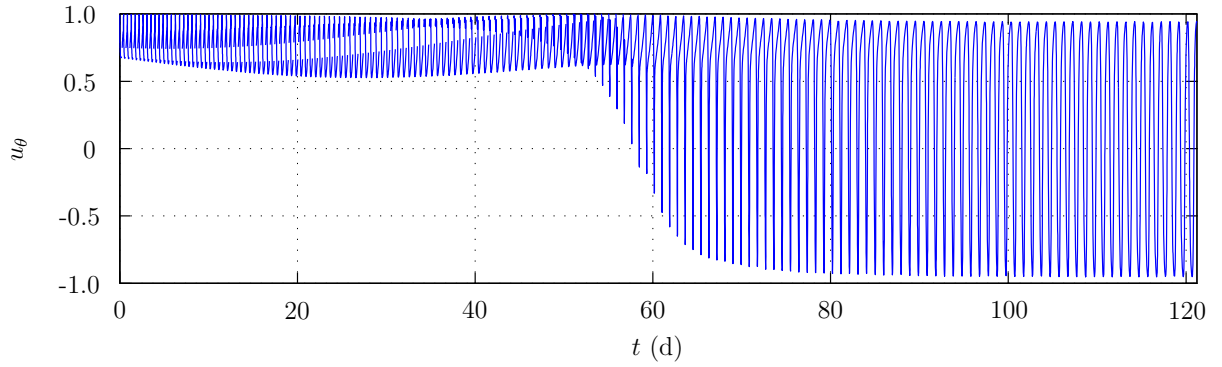
(c)  $i$  vs.  $t$ .

Figure 5:  $a$ ,  $e$ , and  $i$  vs.  $t$  for the GTO-II to GEO transfer.

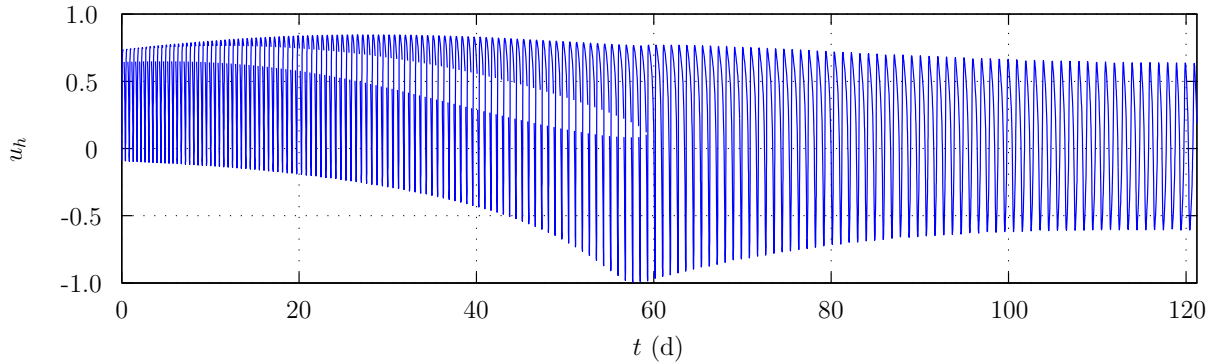
that four segments identify the key features of the optimal control: (1) the first few orbital revolutions of the transfer, (2) the region where  $u_r \approx 0$ , (3) the region where  $u_h$  becomes  $-1$ , and (4) the final orbital revolutions of the transfer.



(a)  $u_r$  vs.  $t$ .



(b)  $u_\theta$  vs.  $t$ .



(c)  $u_h$  vs.  $t$ .

Figure 6:  $\mathbf{u}$  vs.  $t$  for the GTO-II to GEO transfer.

First, Fig. 7a shows the optimal control in the first few orbital revolutions of the transfer, where the gaps in the control are due to the Earth-shadow regions. In this segment of the transfer,  $u_r$  is positive near  $\nu = \pi/2$  and negative near  $\nu = 3\pi/2$  while a positive  $u_\theta$  dominates the thrust direction along all  $\nu$  except just prior to  $\nu = \pi$ . The net effect of  $u_r$  and  $u_\theta$  is then to increase the semi-major axis and to decrease

the eccentricity. Next, it is seen from Fig. 7b that  $di/dt$  [see Eq. (37)] is most negative immediately before to apoapsis. This result is consistent with Fig. 7c where the minimum value of  $di/dt$  coincides with the minimum value of  $\cos(\nu + \omega)u_h$  prior to  $\nu = \pi$ . Because the shadow region appears near apoapsis, the inclination change must be performed elsewhere. In this segment of the transfer, the inclination change is performed most efficiently immediately prior to apoapsis.

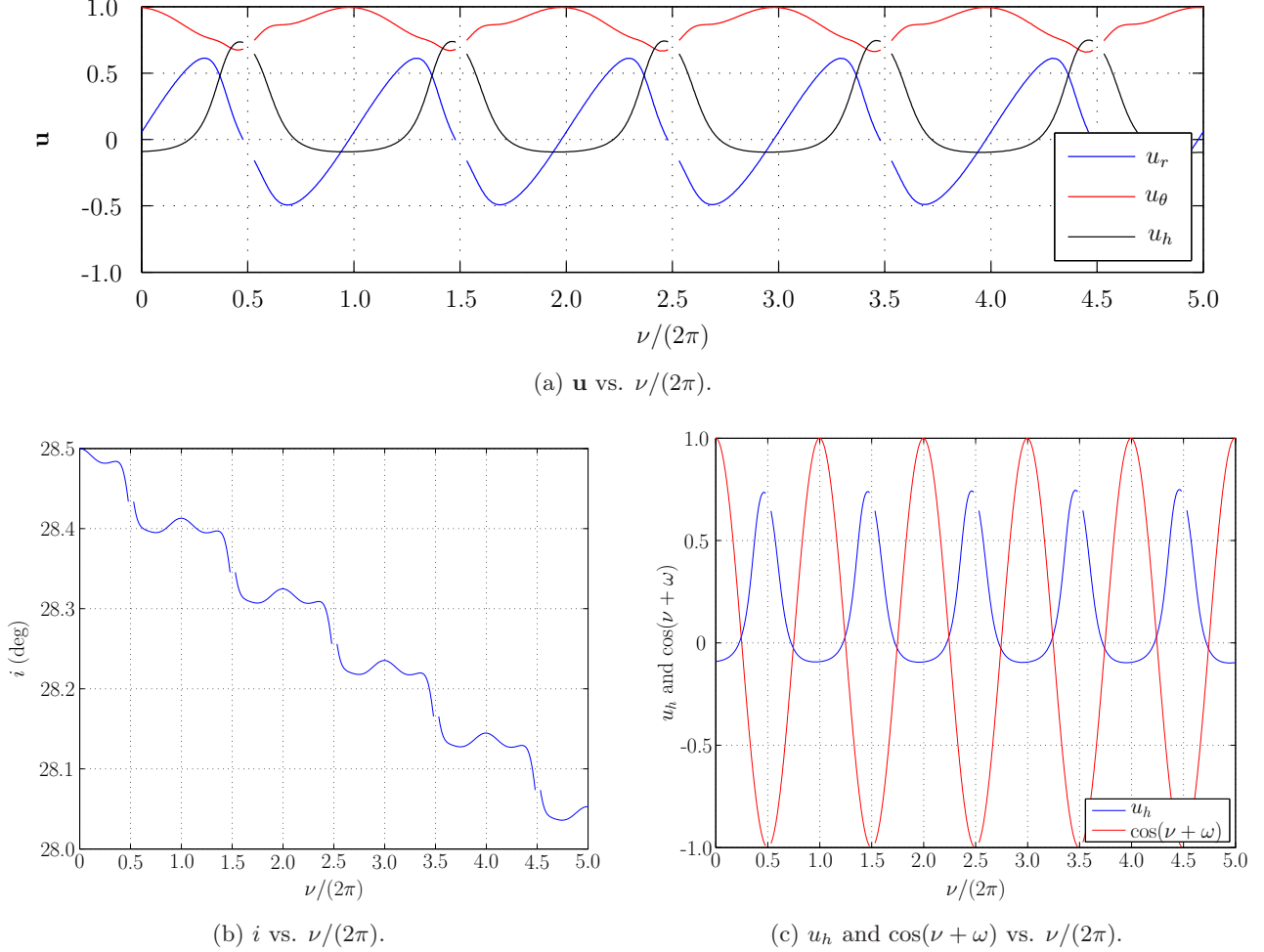


Figure 7:  $\mathbf{u}$ ,  $i$ , and  $\cos(\nu + \omega)$  vs.  $\nu/(2\pi)$  during the first few orbital revolutions of the GTO-II to GEO transfer.

The optimal control in the segment of the transfer where  $u_r \approx 0$  is shown in Fig. 8. For every orbital revolution beyond where  $u_r$  becomes zero (that is, all values beyond  $\nu/(2\pi) = 90.5$ ), the behavior of  $u_r$  changes from its behavior in the first few orbital revolutions such that  $u_r$  is now negative near  $\nu = \pi/2$  and positive near  $\nu = 3\pi/2$ . Since  $u_r \approx 0$  and the thrust direction lies predominately in the positive  $u_\theta$  direction (except just prior to  $\nu = \pi$ ), the overall result is to increase the semi-major axis and to decrease the eccentricity. Similar to the first few orbital revolutions,  $di/dt$  is most negative prior to apoapsis. Even as the shadow region shifts away from apoapsis towards the descending node,  $u_h$  efficiently decreases the

inclination by dominating the thrust direction just before  $\nu = \pi$ .

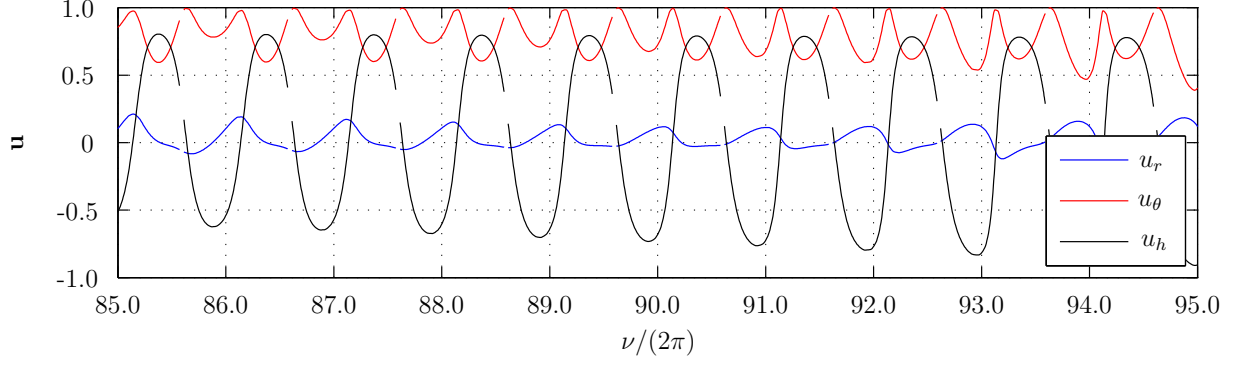


Figure 8:  $\mathbf{u}$  vs.  $\nu/(2\pi)$  when  $u_r \approx 0$  during the GTO-II to GEO transfer.

Next, Fig. 9a shows the optimal control in the segment of the transfer where  $u_h$  becomes  $-1$ . At this particular point in the transfer, the Earth-shadow regions cease to exist (near  $\nu = 99.6$ ) and  $u_r$  is now negative near  $\nu = \pi/2$  and positive near  $\nu = 3\pi/2$ . Moreover,  $u_\theta$  no longer dominates the thrust direction, reaching its most positive value at  $\nu = 5\pi/4$  and a gradually decreasing value at periapsis. The combined effect of  $u_r$  and  $u_\theta$  is then to increase the semi-major axis and to decrease the eccentricity. In Fig. 9b it is seen that  $di/dt$  is negative at periapsis and apoapsis, while Fig. 9c shows that  $\cos(\nu + \omega)u_h$  is negative when  $\nu \approx 0$  and  $\nu \approx 3\pi/4$ . Because the orbital velocity is much smaller at apoapsis than it is at periapsis, the inclination change observed near apoapsis is larger than the change observed near periapsis.

Finally, Fig. 10a shows the optimal control during the last few orbital revolutions of the transfer. Shadow regions do not exist in this segment of the transfer. In the final few orbital revolutions,  $u_r$  is negative near  $\nu = \pi/2$  and positive near  $\nu = 3\pi/2$ , while  $u_\theta$  is positive near  $\nu = 0$  and is negative near  $\nu = \pi$ . Thrusting in this manner increases periapsis and decreases apoapsis and, thus, the overall effect of  $u_r$  and  $u_\theta$  is to increase the semi-major axis and to decrease the eccentricity. From Fig. 10b it is seen that  $di/dt$  is a minimum near  $\nu = 3\pi/4$  and  $\nu = 7\pi/4$ , while Fig. 10c shows that  $\cos(\nu + \omega)u_h$  is negative at  $\nu = 3\pi/4$  and  $\nu = 7\pi/4$ . Because the orbit is nearly circular at the end of the transfer, the rate at which the inclination decreases is essentially the same at  $\nu = 3\pi/4$  and  $\nu = 7\pi/4$ .

### 3.3 Case 3: SSTO to GEO Transfer Results

The results for the selected departure dates are shown in Table 5. While the minimum times obtained were similar for three of the dates, the Summer Solstice departure yielded the best result with a transfer time of 72.60 days and had the largest payload of 1122.68 kg. Moreover, the least desirable departure date was the Vernal Equinox where almost three additional days were required to complete the transfer. The payload delivered, however, was nearly the same for all dates considered.

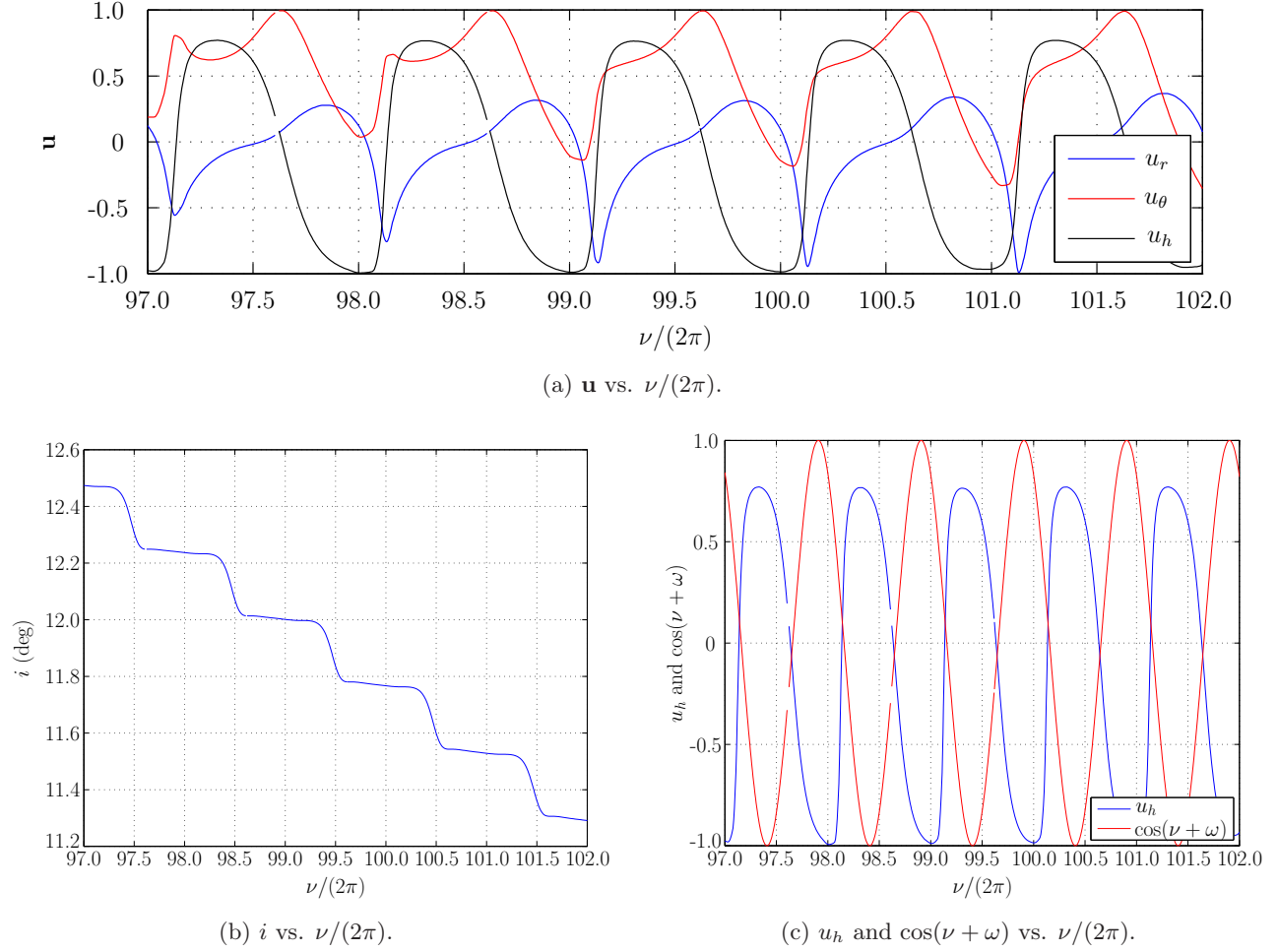
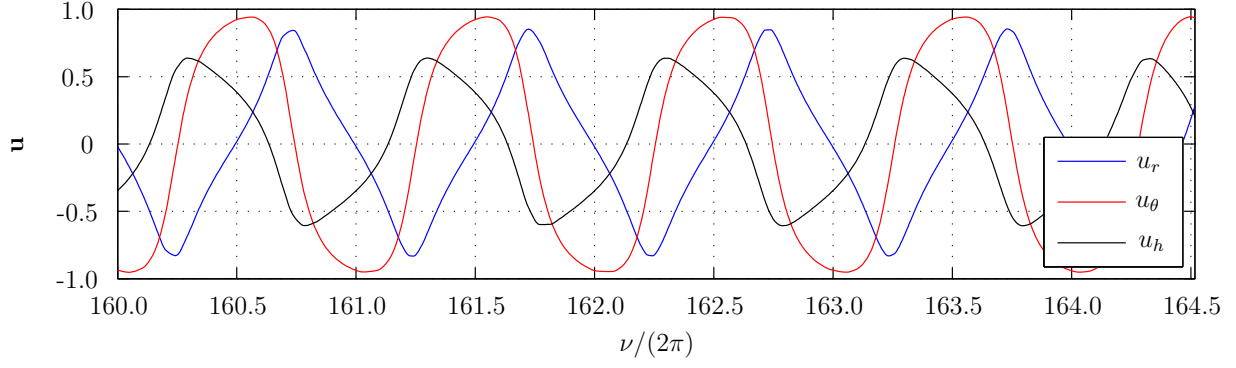


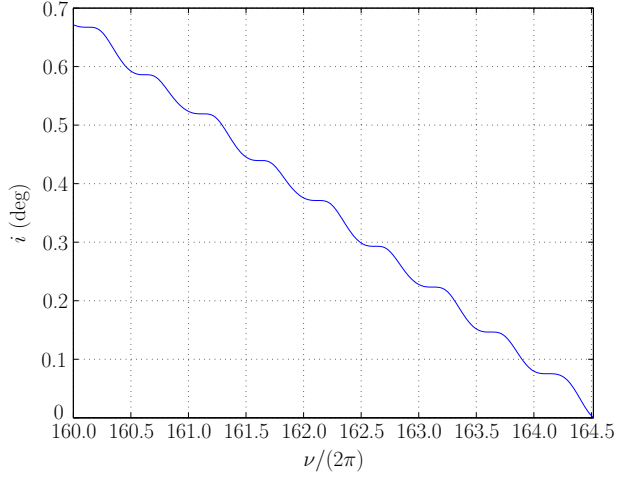
Figure 9:  $\mathbf{u}$ ,  $i$ , and  $\cos(\nu + \omega)$  vs.  $\nu/(2\pi)$  when  $u_h$  becomes -1 during the GTO-II to GEO transfer.

Table 5: Numerical results for SSTO to GEO transfers.

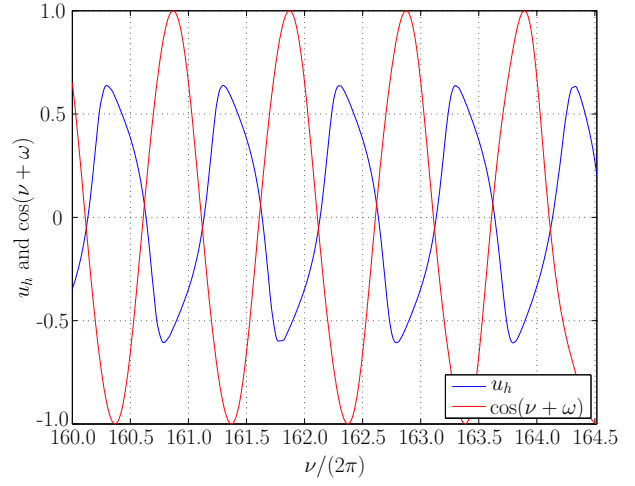
Departure Date	Number of Phases	Time in Shadow (hr)	Final Time (d)	Final Mass (kg)	Final True Longitude (rev)
Vernal Equinox	16	51.47	75.42	1121.42	62.22
Summer Solstice	25	12.21	72.60	1122.68	59.31
Autumnal Equinox	31	15.06	73.49	1121.86	59.23
Winter Solstice	19	12.01	73.06	1122.18	59.24



(a)  $\mathbf{u}$  vs.  $\nu/(2\pi)$ .



(b)  $i$  vs.  $\nu/(2\pi)$ .



(c)  $u_h$  and  $\cos(\nu + \omega)$  vs.  $\nu/(2\pi)$ .

Figure 10:  $\mathbf{u}$ ,  $i$ , and  $\cos(\nu + \omega)$  vs.  $\nu/(2\pi)$  during the final few orbital revolutions of the GTO-II to GEO transfer.

The optimal SSTO to GEO trajectories are shown in ECI Cartesian coordinates  $(x,y,z)$  in Figs. 11-14 for the Vernal Equinox, Summer Solstice, Autumnal Equinox, and Winter Solstice departures, respectively. For each of these four transfers, the shadow regions appear at the beginning of the transfer in key locations throughout the orbit: (1) the Vernal Equinox transfer has shadow regions near apoapsis, (2) the Summer Solstice transfer has shadow regions near the descending node, (3) the Autumnal Equinox transfer has shadow regions near periapsis, and (4) the Winter Solstice transfer has shadow regions near the ascending node. In addition to shadow regions that appear in the beginning of the transfer, the Summer Solstice and Winter Solstice transfers have additional shadow regions that appear in the last few orbital revolutions of the transfers. The locations of the shadow regions are consistent with the fact that spacecraft in GEO will travel through the Earth's shadow in an orbital revolution that occurs between the end of February and the middle of April or between the beginning of September and the middle of October. Because the Summer Solstice transfer takes 72.60 days, the spacecraft will approach GEO near the beginning of September and subsequently travels through the Earth's shadow again as it nears its terminal orbit.

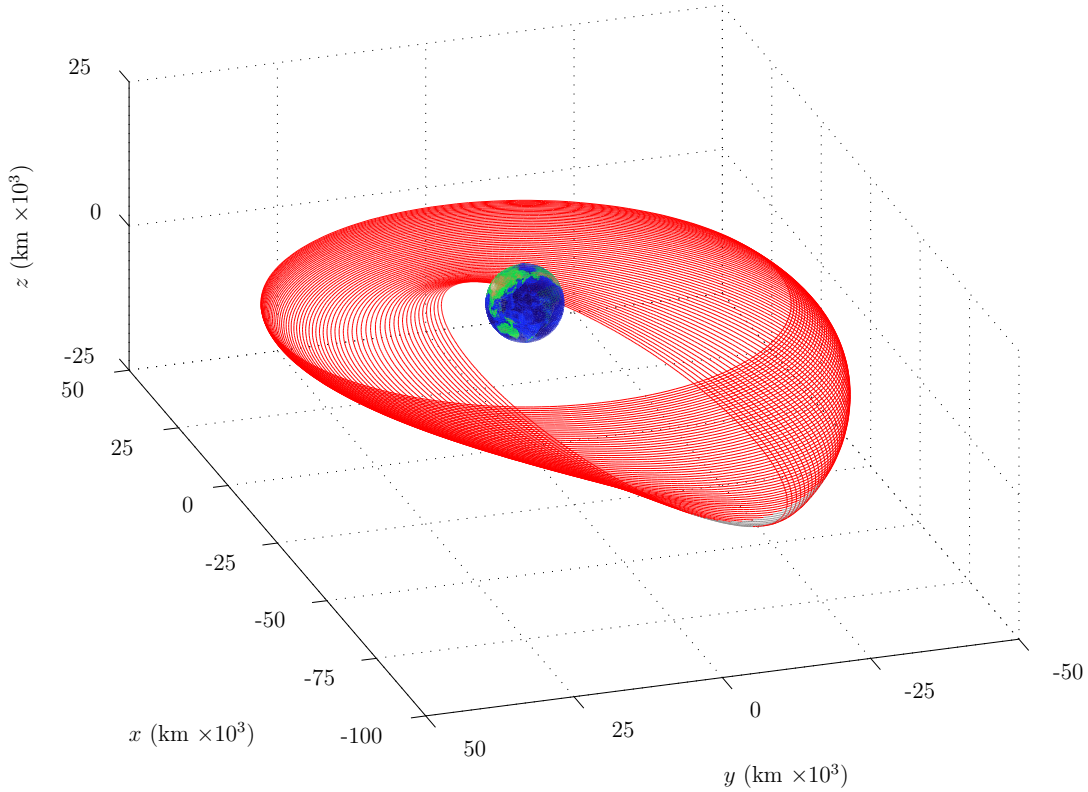


Figure 11: Trajectory for SSTO to GEO transfer with a Vernal Equinox departure.

Figure 15a shows the semi-major axis time history for the Vernal Equinox departure. For the Vernal Equinox, Autumnal Equinox, and Winter Solstice dates, the semi-major axis increases slightly during the first few days of the transfer and then steadily decreases throughout the rest of the transfer. In the Summer Solstice transfer, however, the semi-major axis decreases throughout the entire transfer. For all

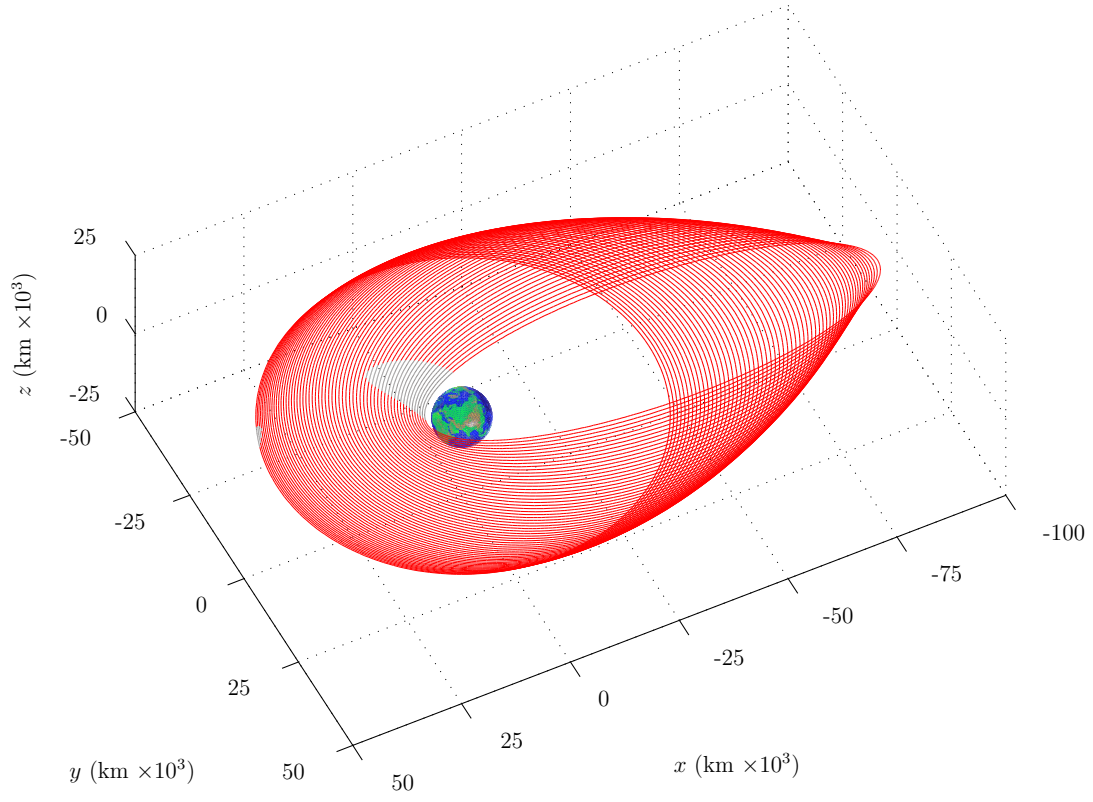


Figure 12: Trajectory for the SSTS to GEO transfer with a Summer Solstice departure.

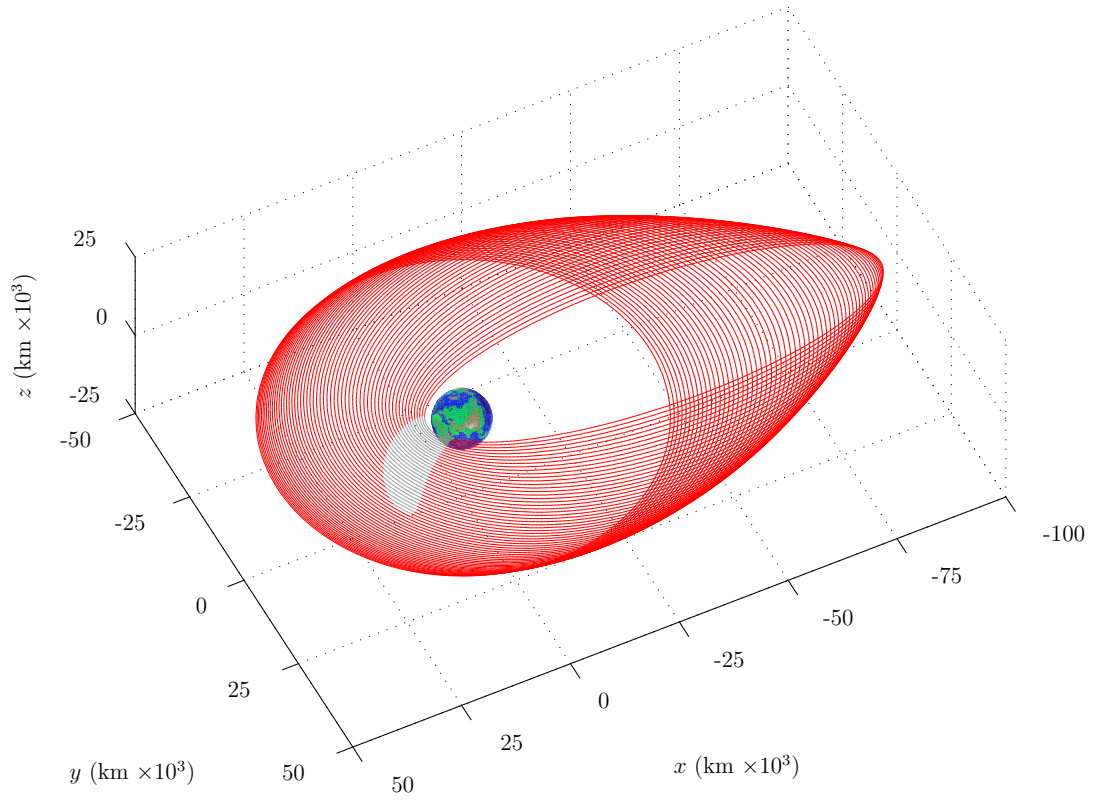


Figure 13: Trajectory for the SSTS to GEO transfer with an Autumnal Equinox departure.



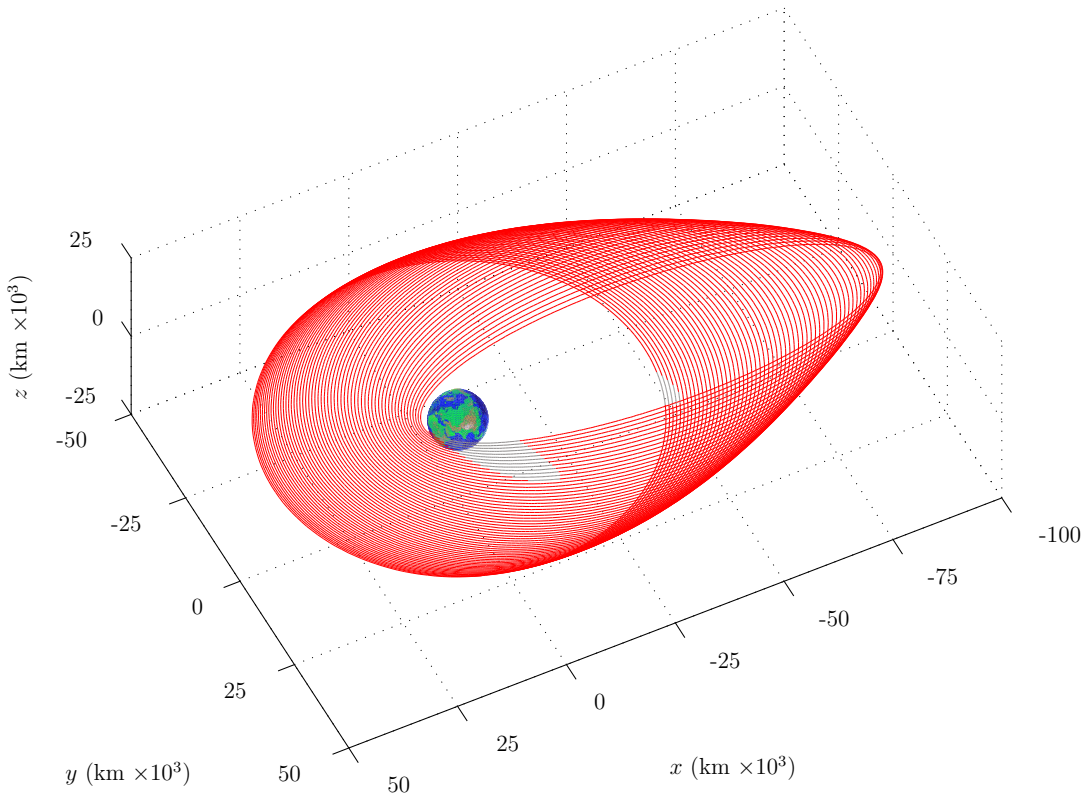
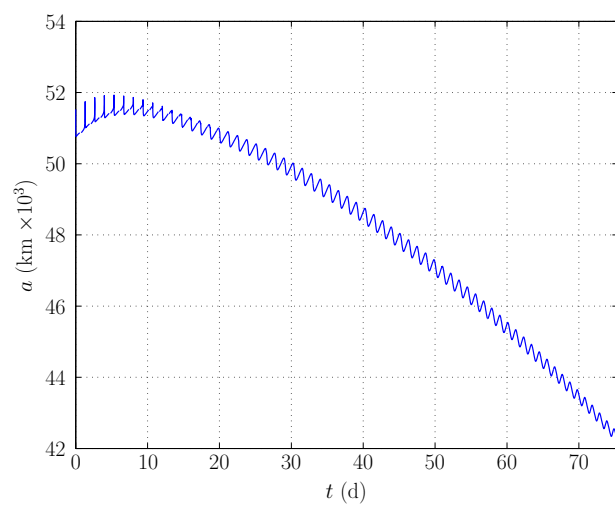


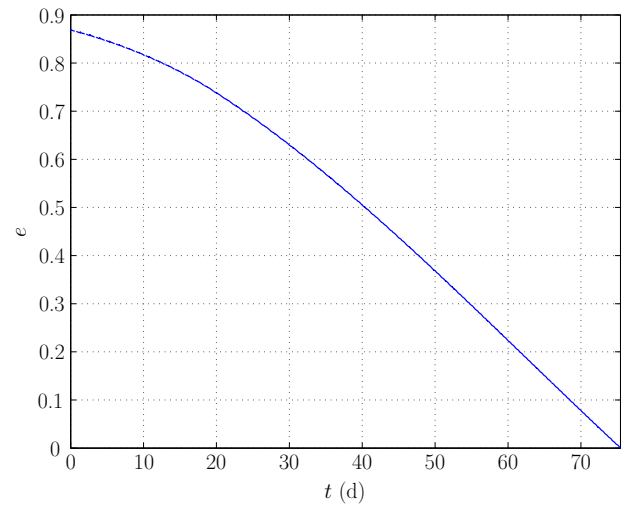
Figure 14: Trajectory for the SSTO to GEO transfer with a Winter Solstice departure.

departure dates considered, the eccentricity and inclination both steadily decrease throughout the transfer as shown in Figs. 15b and 15c, respectively, for the Vernal Equinox departure. The control components  $\mathbf{u} = (u_r, u_\theta, u_h)$  for the Vernal Equinox departure are shown in Fig. 16. While the overall behavior of the control components is fairly similar between all of the departure dates considered, further insight into the structure of the optimal transfers is gained by examining the behavior of the control components during the first few orbital revolutions where the shadow regions are present. The final few orbital revolutions are also examined.

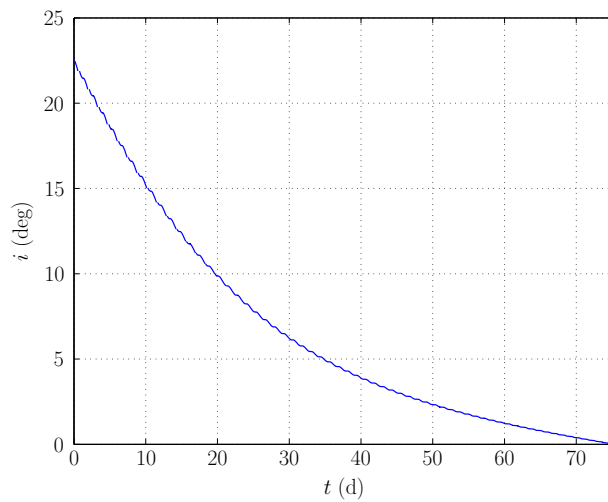
The control components during the first few orbital revolutions for the departure dates considered are shown in Fig. 17. It is seen that the radial component of the control in the initial part of the transfer is similar for all of the departure dates and becomes negative near  $\nu = \pi/2$  and positive near  $\nu = 3\pi/2$ . On the other hand, the tangential component,  $u_\theta$ , and the normal component,  $u_h$ , do not exhibit similar behavior between all departure dates. For all departure dates other than the Vernal Equinox,  $u_\theta$  is negative near  $\nu = 0$  and positive near  $\nu = \pi$ , while  $u_h$  is negative near  $\nu = 0$  and positive near  $\nu = \pi$ . The cyclic behavior of  $u_\theta$  raises periapsis and apoapsis when  $\nu = [\pi/2, 3\pi/2]$ , and lowers periapsis and apoapsis when  $\nu = [3\pi/2, 5\pi/2]$  (including angle wrap). Beginning with the Summer Solstice transfer, shown in Fig. 17b, the effect of  $u_r$  is to lower apoapsis and raise periapsis when  $\nu \in [0, \pi]$ . Because the shadow region appears near  $\nu = 3\pi/2$ , however,  $u_r$  cannot as effectively increase apoapsis and decrease periapsis between



(a)  $a$  vs.  $t$ .

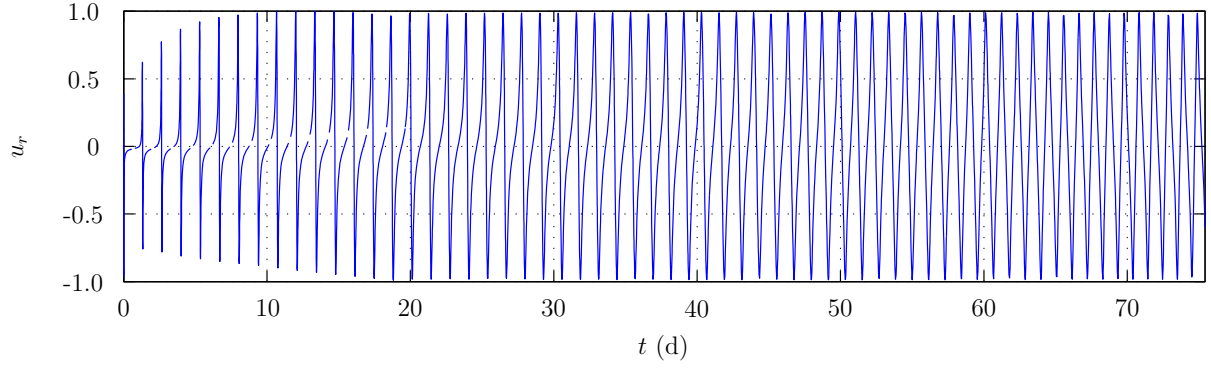


(b)  $e$  vs.  $t$ .

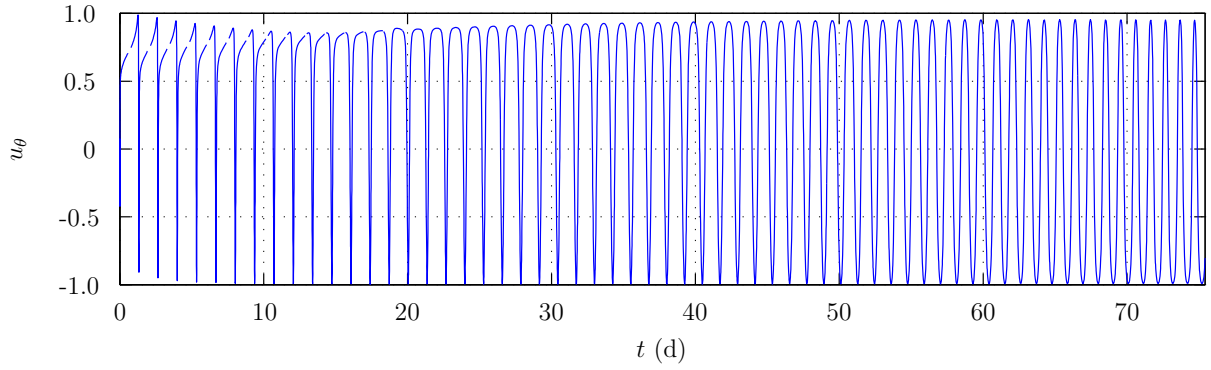


(c)  $i$  vs.  $t$ .

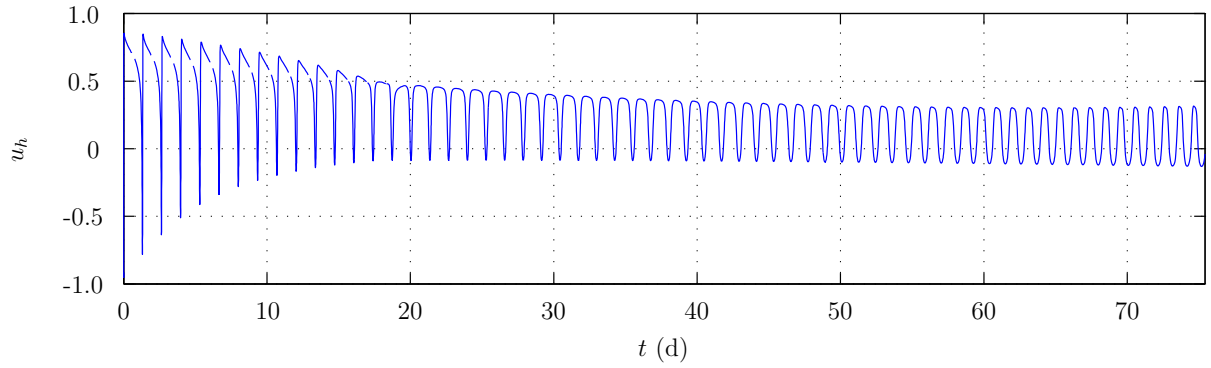
Figure 15:  $a$ ,  $e$ , and  $i$  vs.  $t$  for the SSTO to GEO transfer with a Vernal Equinox departure.



(a)  $u_r$  vs.  $t$ .



(b)  $u_\theta$  vs.  $t$ .

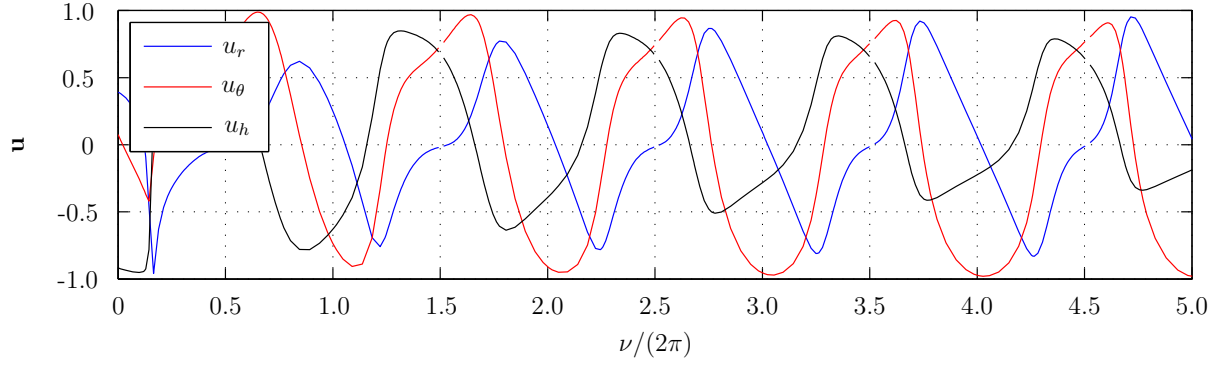


(c)  $u_h$  vs.  $t$ .

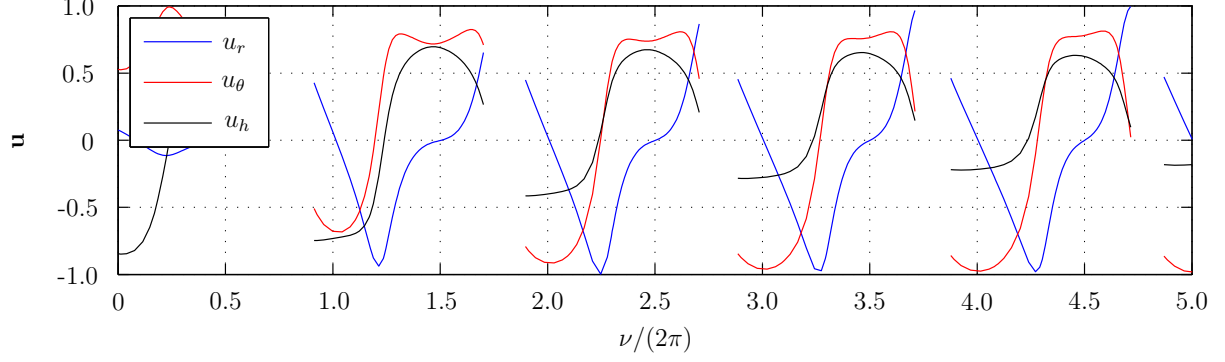
Figure 16:  $\mathbf{u}$  vs.  $t$  for the SSTO to GEO transfer with a Vernal Equinox departure.

$\nu = [\pi, 2\pi]$ . In addition,  $u_\theta$  cannot increase both periapsis and apoapsis. Thus, the overall net effect of  $u_r$  and  $u_\theta$  is to decrease both the semi-major axis and the eccentricity. Next, for the Autumnal Equinox transfer shown in Fig. 17c, the shadow regions appear near periapsis. Because the spacecraft cannot thrust near  $\nu = 0$ ,  $u_\theta$  cannot effectively lower periapsis and apoapsis. The net effect of  $u_r$  and  $u_\theta$ , therefore, is to increase the semi-major axis and to decrease the eccentricity. Examining the Winter Solstice transfer shown in Fig. 17d, the shadow region is initially near  $\nu = \pi/2$  and thus the apoapsis decrease and periapsis increase when  $\nu \in [0, \pi]$  is less than the periapsis decrease or apoapsis increase would be if thrust were available. Furthermore,  $u_\theta$  cannot lower both periapsis and apoapsis. As a result, the net effect of  $u_r$  and  $u_\theta$  is to increase the semi-major axis and to decrease the eccentricity. Recalling that  $u_h$  exhibits similar behavior for the Summer Solstice, Autumnal Equinox, and Winter Solstice transfers, the minimum value of  $di/dt$  corresponds to the minimum value of  $\cos(\nu + \omega)u_h$  at  $\nu = \pi$ . Thus the inclination decreases most rapidly near apoapsis, where the orbital velocity of the spacecraft is the smallest. Finally, for the Vernal Equinox transfer shown in Fig. 17a, the behavior of  $u_\theta$  and  $u_h$  is different from the behavior observed for the other departure dates because the shadow regions appear near apoapsis. For the Vernal Equinox,  $u_\theta$  is most negative near  $\nu = \pi/4$  and most positive near  $\nu = 5\pi/4$ . Even though the behavior of  $u_\theta$  is different for the Vernal Equinox transfer due to the location of the shadow regions near apoapsis,  $u_\theta$  still lowers both periapsis and apoapsis when  $\nu \in [3\pi/2, 5\pi/2]$  and raises both periapsis and apoapsis when  $\nu \in [\pi/2, 3\pi/2]$ . Therefore, the combined effect of  $u_r$  and  $u_\theta$  is to increase the semi-major axis and to decrease the eccentricity. Furthermore, the normal component,  $u_h$ , is positive near  $\nu = 3\pi/4$  and negative near  $\nu = 3\pi/2$ . Different from the other departure dates, the Vernal Equinox transfer cannot perform the inclination change near apoapsis during the first few orbital revolutions of the Vernal Equinox transfer. Examining Fig. 18a,  $di/dt$  is most negative prior to apoapsis, which is consistent with Fig. 18b where the minimum value of  $di/dt$  coincides with the minimum value of  $\cos(\nu + \omega)u_h$  just before to  $\nu = \pi$ .

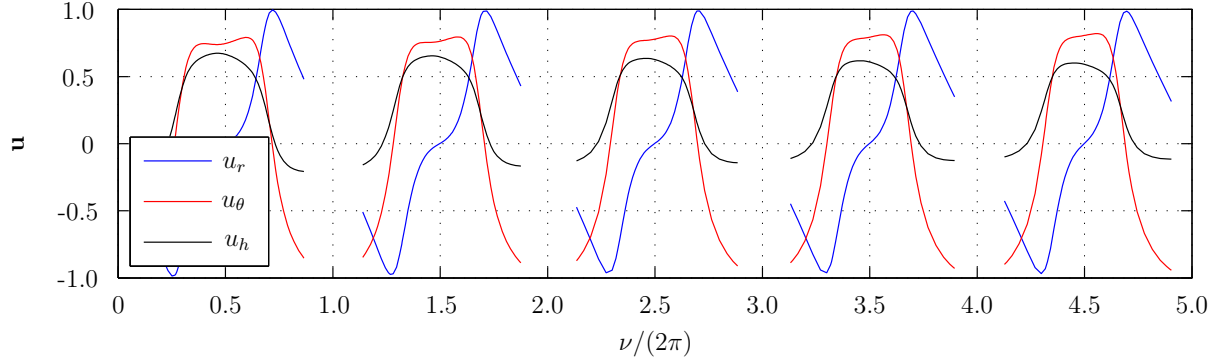
The control components during the final few orbital revolutions of the transfer exhibit similar behavior for all of the departure dates. The control components for the Vernal Equinox departure are shown in Fig. 19. At the end of the transfer,  $u_r$  is negative near  $\nu = \pi/2$  and positive near  $\nu = 3\pi/2$ , while  $u_\theta$  is negative near  $\nu = 0$  and positive near  $\nu = \pi$ . Thrusting in this manner increases periapsis and decreases apoapsis and thus the net effect of  $u_r$  and  $u_\theta$  is to decrease both the semi-major axis and the eccentricity. Lastly,  $u_h$  is negative near  $\nu = 0$  and positive near  $\nu = \pi$ . At this point in the transfer, the orbit is nearly circular and the rate at which the inclination decreases is essentially the same at periapsis and apoapsis.



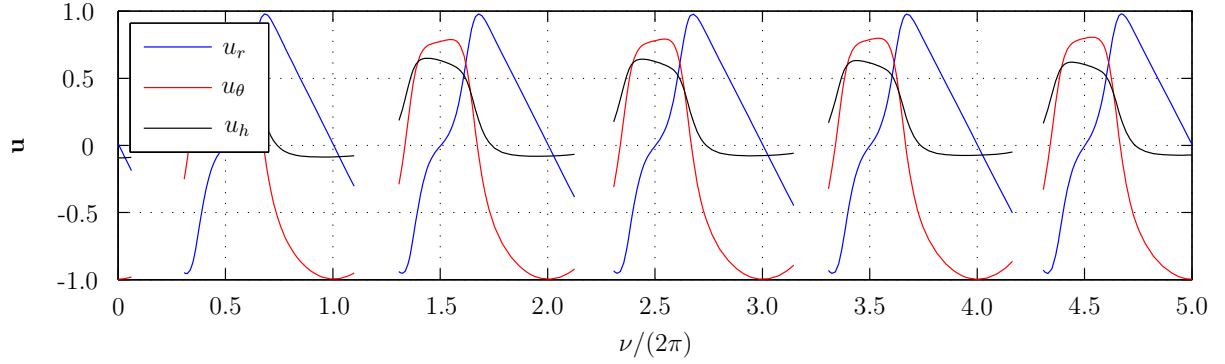
(a) Vernal Equinox.



(b) Summer Solstice.

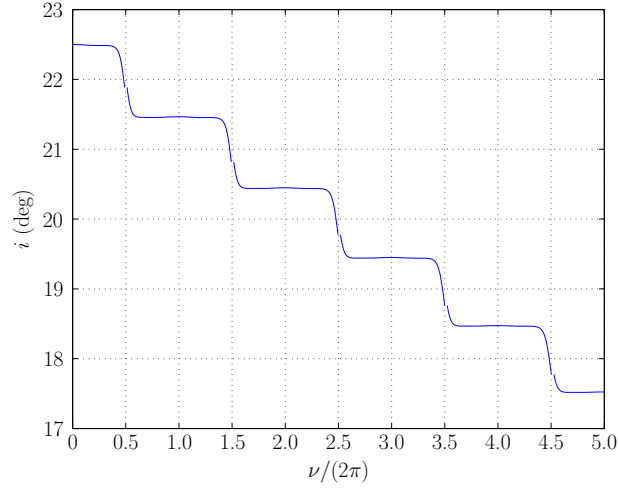


(c) Autumnal Equinox.

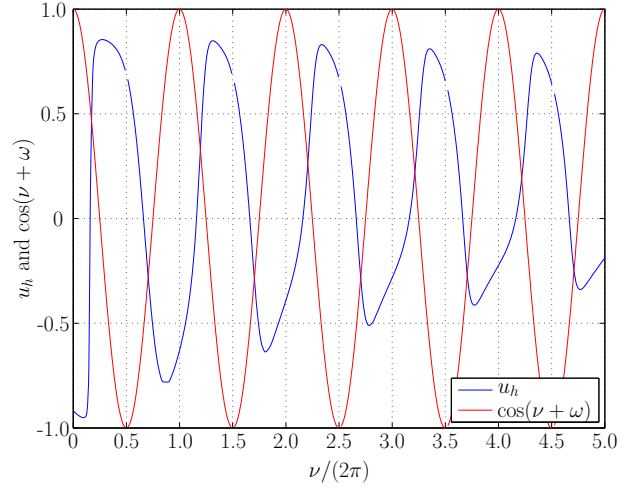


(d) Winter Solstice.

Figure 17:  $\mathbf{u}$  vs.  $\nu/(2\pi)$  during the first few orbital revolutions of the SSTO to GEO transfer with a Vernal Equinox, a Summer Solstice, an Autumnal Equinox, and a Winter Solstice departure.



(a)  $i$  vs.  $\nu/(2\pi)$ .



(b)  $u_h$  and  $\cos(\nu + \omega)$  vs.  $\nu/(2\pi)$ .

Figure 18:  $i$ ,  $u_h$ , and  $\cos(\nu + \omega)$  vs.  $\nu/(2\pi)$  during the first few orbital revolutions of the SSTO to GEO transfer with a Vernal Equinox departure.

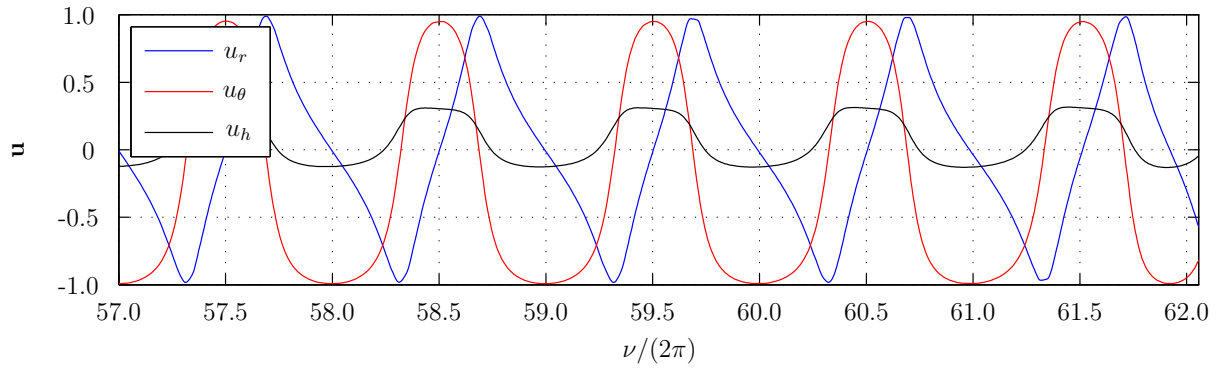


Figure 19:  $\mathbf{u}$  vs.  $\nu/(2\pi)$  during the final few orbital revolutions of the SSTO to GEO transfer with a Vernal Equinox departure.

## 4 Conclusions

The problem of minimum time low-thrust trajectory optimization with eclipsing constraints has been considered. The low-thrust orbit transfer problem is formulated as a multiple-phase optimal control problem. The optimal control problem is solved using a *hp* adaptive Gaussian quadrature orthogonal collocation method. An initial guess is constructed by solving a series of single-phase optimal control problems with continuous thrust. By analyzing these initial guesses, the approximate shadow entrance and exit locations are determined and an intelligent guess is constructed for the multiple-phase optimal control problem with eclipsing constraints. Assuming Keplerian motion during an eclipse, event constraints are enforced that relate the orbit at the terminus of an eclipse to the orbit at the start of an eclipse based on the geometry of the shadow region and eliminate the need to include coast phases in the optimization problem. Three Earth-orbit transfers were chosen to demonstrate the approach developed in this research and the key features of the optimal trajectories were analyzed.

## Acknowledgments

The authors gratefully acknowledge support for this research by the NASA Florida Space Grant Consortium under grant NNX10AM01H, by Space Florida under grant 11-107, and by the National Aeronautics and Space Administration under grant NNX14AN88G.

## References

- [1] Alfano, S. and Thorne, J. D., “Circle-to-Circle, Constant-Thrust Orbit Raising,” *The Journal of Astronautical Sciences*, Vol. 42, No. 1, 1994, pp. 35–45.
- [2] Haissig, C. M., Mease, K. D., and Vinh, N. X., “Minimum-Fuel, Power-Limited Transfers Between Coplanar Elliptic Orbits,” *Acta Astronautica*, Vol. 29, No. 1, January 1993, pp. 1–15.
- [3] Falck, R. D. and Dankanich, J. D., “Optimization of Low-Thrust Spiral Trajectories by Collocation,” *AIAA/AAS Astrodynamics Specialist Conference*, No. 2012-4423, Minneapolis, MN, August 2012.
- [4] Scheel, W. A. and Conway, B. A., “Optimization of Very-Low-Thrust, Many-Revolution Spacecraft Trajectories,” *Journal of Guidance, Control, and Dynamics*, Vol. 17, No. 6, November-December 1994, pp. 1185–1192.
- [5] Haberkorn, T., Martinon, P., and Gergaud, J., “Low-Thrust Minimum-Fuel Orbital Transfer: A Homotopic Approach,” *Journal of Guidance, Control, and Dynamics*, Vol. 27, No. 6, 2004.
- [6] Betts, J. T., “Very low-thrust trajectory optimization using a direct SQP method,” *Journal of Computational and Applied Mathematics*, Vol. 120, No. 1-2, August 2000, pp. 27–40.
- [7] Ross, I. M., Gong, Q., and Sekhavat, P., “Low-Thrust, High-Accuracy Trajectory Optimization,” *Journal of Guidance, Control, and Dynamics*, Vol. 30, No. 4, July-August 2007, pp. 921–933.

- [8] Graham, K. F. and Rao, A. V., “Minimum-Time Trajectory Optimization of Multiple Revolution Low-Thrust Earth-Orbit Transfers,” *Journal of Spacecraft and Rockets*, Vol. 52, No. 3, May-June 2015, pp. 711–727.
- [9] Kluever, C. A. and Oleson, S. R., “Direct Approach for Computing Near-Optimal Low-Thrust Earth-Orbit Transfers,” *Journal of Spacecraft and Rockets*, Vol. 35, No. 4, July-August 1998, pp. 509–515.
- [10] Gao, Y., “Near-Optimal Very Low-Thrust Earth-Orbit Transfers and Guidance Schemes,” *Journal of Guidance, Control, and Dynamics*, Vol. 30, No. 2, March-April 2007, pp. 529–539.
- [11] Yang, G., “Direct Optimization of Low-thrust Many-revolution Earth-orbit Transfers,” *Chinese Journal of Aeronautics*, Vol. 22, No. 4, August 2009, pp. 426–433.
- [12] Neta, B. and Vallado, D., “On Satellite Umbra/Penumbra Entry and Exit Positions,” *Journal of the Astronautical Sciences*, Vol. 46, No. 1, 1998, pp. 91–104.
- [13] Geffroy, S. and Epenoy, R., “Optimal low-thrust transfers with constraints—generalization of averaging techniques,” *Acta Astronautica*, Vol. 41, No. 3, 1997, pp. 133–149.
- [14] Ferrier, C. and Epenoy, R., “Optimal Control for Engines with Electro-Ionic Propulsion Under Constraint of Eclipse,” *Acta Astronautica*, Vol. 48, No. 4, 2001, pp. 181–192.
- [15] Kechichian, J. A., “Low-Thrust Eccentricity-Constrained Orbit Raising,” *Journal of Spacecraft and Rockets*, Vol. 35, No. 3, May-June 1998, pp. 327–335.
- [16] Kechichian, J. A., “Orbit Raising with Low-Thrust Tangential Acceleration in Presence of Earth Shadow,” *Journal of Spacecraft and Rockets*, Vol. 35, No. 4, July-August 1998, pp. 516–525.
- [17] Kechichian, J. A., “Low-Thrust Inclination Control in Presence of Earth Shadow,” *Journal of Spacecraft and Rockets*, Vol. 35, No. 4, July-August 1998, pp. 526–532.
- [18] Betts, J. T., “Optimal Low Thrust Orbit Transfers with Eclipsing,” *Optimal Control Applications and Methods*, DOI: 10.1002/oca.2111, 2014.
- [19] Benson, D. A., Huntington, G. T., Thorvaldsen, T. P., and Rao, A. V., “Direct Trajectory Optimization and Costate Estimation via an Orthogonal Collocation Method,” *Journal of Guidance, Control, and Dynamics*, Vol. 29, No. 6, November-December 2006, pp. 1435–1440.
- [20] Huntington, G. T., Benson, D. A., and Rao, A. V., “Optimal Configuration of Tetrahedral Spacecraft Formations,” *Journal of the Astronautical Sciences*, Vol. 55, No. 2, April-June 2007, pp. 141–169.
- [21] Huntington, G. T. and Rao, A. V., “Optimal Reconfiguration of Tetrahedral Spacecraft Formations Using the Gauss Pseudospectral Method,” *Journal of Guidance, Control, and Dynamics*, Vol. 31, No. 3, May-June 2008, pp. 141–169.
- [22] Rao, A. V., Benson, D. A., Darby, C. L., Francolin, C., Patterson, M. A., Sanders, I., and Huntington, G. T., “Algorithm 902: GPOPS, A Matlab Software for Solving Multiple-Phase Optimal Control Problems Using the Gauss Pseudospectral Method,” *ACM Transactions on Mathematical Software*, April-June 2010.
- [23] Garg, D., Patterson, M. A., Hager, W. W., Rao, A. V., Benson, D. A., and Huntington, G. T., “A Unified Framework for the Numerical Solution of Optimal Control Problems Using Pseudospectral Methods,” *Automatica*, Vol. 46, No. 11, November 2010, pp. 1843–1851.



- [24] Garg, D., Patterson, M. A., Darby, C. L., Francolin, C., Huntington, G. T., Hager, W. W., and Rao, A. V., “Direct Trajectory Optimization and Costate Estimation of Finite-Horizon and Infinite-Horizon Optimal Control Problems via a Radau Pseudospectral Method,” *Computational Optimization and Applications*, Vol. 49, No. 2, June 2011, pp. 335–358.
- [25] Patterson, M. A., Hager, W. W., and Rao, A. V., “A  $ph$  Mesh Refinement Method for Optimal Control,” *Optimal Control Applications and Methods*, Vol. 36, No. 4, July–August 2015, pp. 398–421.
- [26] Patterson, M. A. and Rao, A. V., “GPOPS – III: A MATLAB Software for Solving Multiple-Phase Optimal Control Problems Using  $hp$ -Adaptive Gaussian Quadrature Collocation Methods and Sparse Nonlinear Programming,” *ACM Transactions on Mathematical Software*, Vol. 41, No. 1, October 2014, pp. 1:1–1:37.
- [27] Walker, M. J. H., Owens, J., and Ireland, B., “A Set of Modified Equinoctial Orbit Elements,” *Celestial Mechanics*, Vol. 36, No. 4, 1985, pp. 409–419.
- [28] Prussing, J. E. and Conway, B. A., *Orbital Mechanics*, Oxford University Press, 2nd ed., 2013.
- [29] U.S. Naval Observatory and H.M. Nautical Almanac Office, *The Astronomical Almanac for the Year 2013*, United Kingdom Hydrographic Office, 2012.
- [30] Longo, C. R. O. and Rickman, S. L., “Method for the Calculation of Spacecraft Umbra and Penumbra Shadow Terminator Points,” Tech. rep., NASA, April 1995.
- [31] Biegler, L. T. and Zavala, V. M., “Large-Scale Nonlinear Programming Using IPOPT: An Integrating Framework for Enterprise-Wide Optimization,” *Computers and Chemical Engineering*, Vol. 33, No. 3, March 2008, pp. 575–582.
- [32] Patterson, M. A. and Rao, A. V., “Exploiting Sparsity in Direct Collocation Pseudospectral Methods for Solving Optimal Control Problems,” *Journal of Spacecraft and Rockets*, Vol. 49, No. 2, March–April 2012, pp. 364–377.
- [33] Francolin, C. C., Benson, D. A., Hager, W. W., and Rao, A. V., “A  $ph$  Mesh Refinement Method for Optimal Control,” *Optimal Control Applications and Methods*, Vol. 36, No. 4, July–August 2015, pp. 381–397.
- [34] Kluever, C. A., “Low-Thrust Trajectory Optimization Using Orbital Averaging and Control Parameterization,” *Spacecraft Trajectory Optimization*, edited by B. A. Conway, Cambridge University Press, New York, NY, 1st ed., 2010, pp. 112–138.
- [35] Chobotov, V. A., *Orbital Mechanics*, American Institute of Aeronautics and Astronautics, Inc., 1991.
- [36] Sackett, L. L., Malchow, H. L., and Edelbaum, T. N., “Solar Electric Geocentric Transfer With Attitude Constraints: Analysis,” Tech. Rep. CR-134927, NASA, August 1975.